Collagen Pre-strain Discontinuity at the Cartilage - Bone Interface

Waqas Badar[1], Husna Ali[1], Olivia N Brooker[1], E. Newham[1], Tim Snow[2], Nicholas J Terrill[2], Gianluca Tozzi[3], Peter Fratzl[4], Martin M Knight[1], and Himadri S Gupta[1]

[1] Institute of Bioengineering and School of Engineering and Material Science, Queen Mary University of London, London, E1 4NS, United Kingdom
[2] Harwell Science and Innovation Campus, Diamond Light Source, Harwell, Didcot, OX11 10 0DE, United Kingdom
[3] School of Engineering, London South Bank University, London SE1 0AA, United Kingdom
[4] Department of Biomaterials, Max-Planck-Institute of Colloids and Interfaces, Potsdam Wissenschaftspark, Golm, Germany

Abstract

The bone-cartilage unit (BCU) is a universal feature in diarthrodial joints, which is mechanically-graded and subjected to shear and compressive strains. Changes in the BCU have been linked to osteoarthritis progression. Here we report existence of a physiological internal strain gradient (pre-strain) across the BCU at the ultrastructural scale of the extracellular matrix constituents, specifically the collagen fibril. We use X-ray scattering that probes changes in the axial periodicity of fibril-level D-stagger of tropocollagen molecules in the matrix fibrils, as a measure of microscopic pre-strain. We find that mineralized collagen nanofibrils in the calcified plate are in tensile pre-strain relative to the underlying trabecular bone. This behaviour contrasts with the previously accepted notion that fibrillar pre-strain (or D-stagger) in collagenous tissues always reduces with mineralization, via reduced hydration and associated swelling pressure. Within the calcified part of the BCU, a finer-scale gradient in pre-strain (0.6% increase over ~50μm) is observed. The increased fibrillar pre-strain is linked to prior research reporting large tissue-level residual strains under compression. The findings may have biomechanical adaptative significance: higher in-built molecular level resilience/damage resistance to physiological compression, and disruption of the molecular-level pre-strains during remodelling of the BCI may be potential factors in osteoarthritis-based degeneration.

Corresponding Author
Himadri S. Gupta (h.gupta@qmul.ac.uk)
Institute of Bioengineering and School of Engineering and Material Science, Queen Mary University of London, London, E1 4NS, United Kingdom

Keywords: bone-cartilage unit, graded biomaterials, collagen fibrils, small-angle X-ray scattering, synchrotron X-ray imaging

Introduction

The bone-cartilage unit (BCI) plays a crucial biomechanical role in enabling pain-free articulation and smooth transmission of shear and compressive stresses across diarthrodial joints [1]. Structural breakdown and alterations in bone-cartilage cellular communication at the BCI has been proposed as a key early-stage marker for osteoarthritis [2]. Osteoarthritis is a debilitating musculoskeletal degenerative condition, with over 300 million people affected [3] and a global prevalence over 20% for individuals over 40 [4]. Development of structural biomarkers for early-stage degeneration in interfaces like the BCI would enable early diagnosis and better therapies [5]. As these changes will originate at the molecular- and supramolecular level, understanding the functional design of such interfaces at the nanoscale in both healthy and degenerative conditions is of importance.

The BCI, like other biological interfaces[6], exhibits gradients in both structure and mechanical properties, resulting in gradients in strain during physiological activity. On one side, there is a layer of AC with depth-dependent gradients in fibre orientation (first described by the Benninghof architecture [7]), type II collagen/proteoglycan content ratios, and hydration [8], and (more recently identified) nanoscale collagen fibrillar pre-strain and intramolecular disorder [9]. As shown in **Figure 1**, collagen fibrils in the AC traverse a tidemark into a layer of calcified cartilage of [10,11], enabling a firm anchorage of the AC cartilage to the underlying subchondral bone. Below the subchondral bone is the more open spongy or trabecular bone network. Scanning X-ray scattering and electron microscopy measurements on the calcified mineral phase in the calcified plate (the combined calcified cartilage and subchondral bone) have revealed gradients in mineral composition [12], crystallinity, and size [10], and recently, differences in the mineral crystallite thickness between healthy and osteoarthritic patients[11,13]. The gradient in compressive properties from cartilage (1-10MPa) to subchondral bone (GPa) reduces high interfacial shear stresses which could otherwise lead to cracks and delamination between the softer cartilage and the stiffer bone. Even with graded mechanical properties, physiological loading still induces high apparent strains of up to 5% in the calcified cartilage interface, measured using DVC [14]. Such a combination of high *in vivo* loading along with gradients across mechanically

dissimilar materials requires a structurally optimized design at the material level, to prevent microcrack propagation [15] and enable energy absorption during loading.

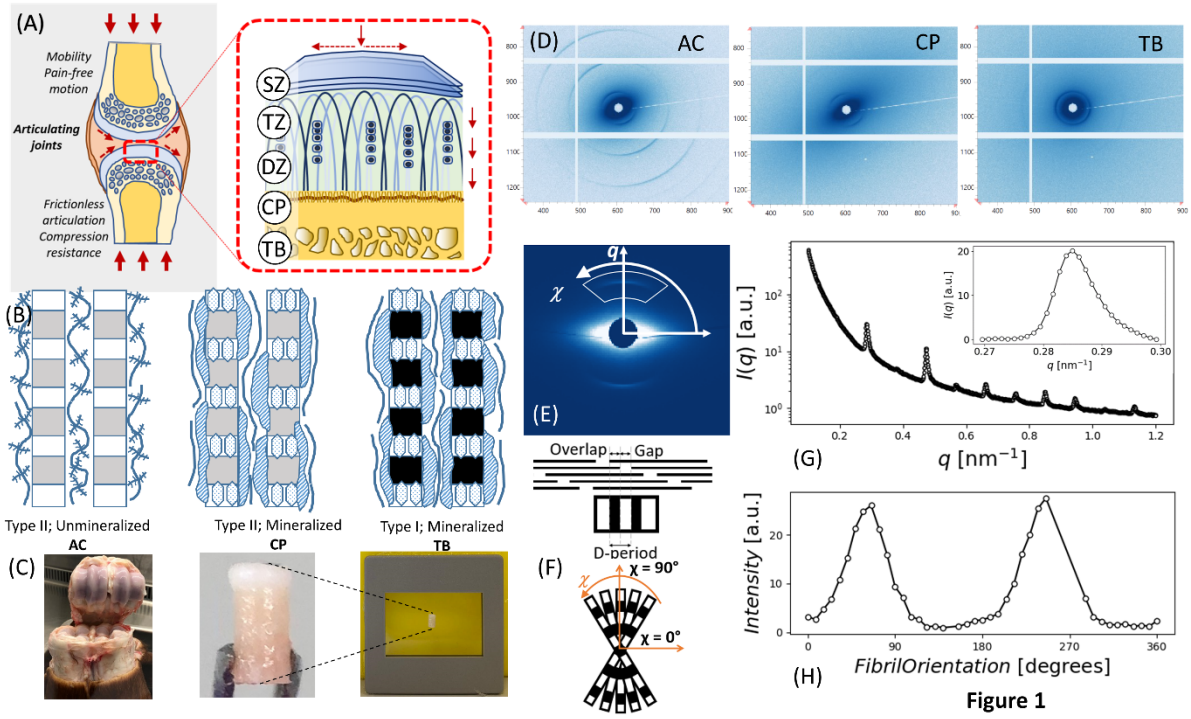

Figure 1: *Bovine BCU explants and small angle X-ray scattering (SAXS) data analysis:* (A) Schematic of joint structure showing the collagen fibril orientation from parallel to the articulating surface in the superficial zone, to vertical in the deep zone and calcified plate. Dashed arrows indicate, schematically, the directions of shear (horizontal) and compressive (vertical) stresses. *Abbreviations for region classification*: SZ: Superficial zone; TZ: transitional zone; DZ: deep zone: CP: calcified plate, TB: trabecular bone (B) Fibrillar microstructure in AC, CP, and TB zones. Type II collagen fibrils are found in AC and CP with mineral particles growing in the gap regions of the CP, whereas type I is found in TB. (C) Bone-cartilage unit (BCU) cores of 5mm length and 2mm diameter extracted from bovine metacarpophalangeal joints and placed in cassette holder for SAXS scanning while kept hydrated. (D) 2D SAXS patterns from AC, CP, and TB. Low diffuse small-angle X-ray scattering (SAXS) with clear peaks and oriented ellipse in AC, high diffuse SAXS with average peaks and oriented ellipse in CP and high diffuse SAXS with average peaks and no orientation for ellipse in TB. (E) Azimuthal and radial integration to get the I(q) and I(χ) profiles to infer nano structural parameters (D-period, fibrillar orientation and degree of alignment). (F) Fibril schematic: Collagen D-period, characterised by the repeating gap-overlap regions causes by the staggered fibril stacking and fibrillar orientation. (G) I(q) plot, showing peaks due to collagen D-period, particularly clear at the 3rd and 5th order after azimuthally integration (0-360°) around the diffraction pattern for the q-radial range 0.1-1.2nm^{-1}. Right top plot is 3rd order collagen peak after background subtraction. (H) I(χ) profiles after corrected intensity with Gaussian model fitting to the peak. Gaussian fitting was used to infer parameters (fibril orientation and ρ).

At this material level, the extracellular matrix (ECM) of the BCI in articular cartilage, the calcified plate and trabecular bone is essentially a collagen fibrillar composite, with a variable composition of the extrafibrillar phase (**Figure 1**): glycosaminoglycan (GAG)/proteoglycan(PG) rich in articular cartilage, while predominantly mineralized (carbonated apatite) in the calcified plate and trabecular bone [16,17]. Biochemically, articular cartilage and calcified cartilage contain predominantly Type II collagen versus Type I collagen in the subchondral and trabecular bone. Both fibril types exhibit a characteristic D-banding periodicity (D~65-67 nm) which is detectable with methods such as small-angle X-ray scattering (SAXS) [18,19] and atomic force microscopy [20]. Shifts in the D-period have been linked to fibril strain in bone, tendon, and cartilage [18,21–23], although recent work highlights the need to consider intra-fibril tilt as well, in tissues like cornea [22,24].

Internal strains and stresses in the fibril phase (both at equilibrium and under loading) are expected to be crucial for structural integrity, joint function and mechanobiological stimuli. The fibril composite in cartilage can be considered as a pre-stressed hydrogel, where swelling pressure exerted by the hydrated GAG/PG is restrained by the collagen fibres leading to tensile pre-strain on the collagen fibrils, identified by an increase in D-period. Recently, our synchrotron X-ray scattering analysis of the ECM nanostructure in the articular cartilage has shown that this fibrillar pre-strain exhibits an increase from the superficial/transitional to the deep zone by ~1% (corresponding to ~5 MPa) adjacent to the calcified plate in the order of [9]. Such nanoscale gradients are associated with the well-established micro- and macro-level gradients in fibril orientation from parallel to perpendicular to the joint surface known previously [25]. Under compressive loading or synthetic ageing, we demonstrated that these fibrillar gradients in pre-strain are disrupted, indicating the gradients play a mechanically important role in the stabilisation of articular cartilage [9]. However, a limitation of the previous study [9] was that the mechanically crucial calcified plate and underlying bone was not considered, as biopsies were taken by cutting the tissue at the BCI, in common with many other studies measuring the mechanical properties of cartilage explants *ex-vivo*. Indeed, mineralized collagen (as found in the calcified plate and trabecular bone) has usually a lower D-period than unmineralized (as in articular cartilage), which has been explained via loss of water inside the fibril [26–28]. The pre-strain thus increases from the

120 transitional/superficial to deep zone cartilage [9], lying adjacent to the underlying mineralized tissue
121 with a putatively lower D-period. The calcified plate is subject to significant tissue-level and microscale
122 strains in loading [14]. However, the corresponding ultrastructural D-period variation in the calcified
123 plate (relative to the articular cartilage and trabecular bone) has not been measured.
124
125 This present study aims to measure the gradient in pre-strain in collagen D-period and related
126 ultrastructural properties in the BCI, focusing on the calcified plate, to better characterise this
127 biomechanical interface critical for healthy joint function. A bovine model of the bone-cartilage
128 interface from metacarpophalangeal joints is used [9,18]. High brilliance synchrotron X-ray SAXS
129 mapping, in the fast fly-scan modes, allows relatively rapid data acquisition across micro- and
130 macroscale tissue regions. The high X-ray flux at synchrotrons enable localized measurements with a
131 micro-beam, necessary to detect micron-scale variation of nanoscale ECM parameters. We carry out
132 SAXS mapping with multiple (three) spatial resolutions 1) across the entire articular cartilage, calcified
133 plate, and trabecular bone, and 2) focused on the articular cartilage and calcified plate, and 3) a high-
134 resolution mapping of the calcified plate region. Our results will identify whether potentially
135 mechanically important equilibrium or pre-strain gradients exist at the ECM level, helping establish
136 baselines for deviations in osteoarthritis and other musculoskeletal degeneration.
137

138 Materials and Methods

139 **Sample preparation:**

140 Bone-cartilage unit (BCU) explants were extracted from a metacarpophalangeal (MCP) joint (**Figure**
141 **1C)**, of freshly slaughtered adult bovine steers (16-24 months of age), delivered by the local abattoir.
142 Bovine cartilage was selected for use in the experiment, as it is both widely available, has less variability
143 as compared to human cartilage samples and is the next best biomechanical approximation of human
144 cartilage[29]. The intact joints were washed with biological detergent followed by immersion in
145 disinfectant (Chemgene) for 15 minutes (this procedure did not affect the internal cartilage and bone
146 tissue as the joints were intact). Joints were then opened using sterile disposable scalpel blades (Swann

147 Morton) in a biohazard safety cabinet. The metacarpal bone was removed, and two metacarpal condyles
148 were isolated from each joint using a high high-speed saw. Extracting intact bone-cartilage cores
149 required a custom sample-preparation process; a method inspired by the work of Aspden and co-
150 workers was used [30]. First, each condyle was placed in a custom-designed 3D-printed holder with an
151 axis of rotation matching that of the condyle flexion axis. A bench drill (Axminster), with a diamond
152 coated coring drill bit was used to produce cores of 2mm diameter, under constant irrigation. The
153 condyle was rotated around the sample-holder axis so that, at each extraction point on the condyle, the
154 drill-face was incident locally normal to the condylar surface; this ensured flat cylindrical samples. The
155 drill was used to core to a 5 mm-depth at five locations on the proximal surface of each condyle. To
156 complete the extraction, the intact condyle was removed from the 3D-printed holder, and the reverse
157 face of the condylar section was abraded continuously with a high-speed Dremel rotary tool equipped
158 with a burring-bit, until each core detached. Both drilling systems were used with constant phosphate
159 buffered saline solution (PBS) (Sigma-Aldrich, Poole, UK) irrigation, with the drilling advancing
160 slowly to minimize heat and mechanical damage. Finally, the extracted cores were cut to an equal length
161 of 5mm by removing excess TB, using a Buehler IsoMet low-speed saw and a 3D printed sample holder
162 under constant irrigation. Final cores, as shown in **Figure 1C,** were placed in Eppendorf tubes with
163 Dulbecco's Modified Eagle's Medium – low glucose (DMEM) (Sigma-Aldrich, Poole, UK), and stored
164 at -20°C until the experiments were conducted at Diamond Light Source (DLS).
165
166 **SAXS measurement protocols:**
167 SAXS scanning of the BCU were performed at beamline I22 [31], Diamond Light Source (DLS,
168 Harwell Science and Innovation Campus, Didcot, UK). The beam size at the sample was measured to
169 be 20μm, beam energy of 14keV and the sample to detector distance at 5.8m. The samples were
170 mounted in film cassette windows (**Figure 1C**), which were sealed using a bilayer Kapton film
171 arrangement with enclosed PBS, to ensure hydration over the duration of the SAXS scan. SAXS
172 scanning was performed with a Pilatus 2M detector [32] (pixel size 172 μm; resolution 1475 × 1679
173 pixels) with an exposure time of 1s for each SAXS measurement. SAXS scans were carried out in "fly-
174 scan" mode where the sample-stage moves continuously during the measurement; this ensures rapid

175 data collection whilst still maintaining spatial registration. Three different SAXS scan settings were
176 used:
177 *Regular scan*: For n=6 samples, a rectangular 2D area scan of 2.6mm (vertical (y)) × 0.8mm (horizontal
178 (x)) was performed with 40 µm increments in both x- and y-direction across the BCU, which included
179 the full AC and CP tissue but only a part (1.36mm) of the ~4 mm long TB region.
180 *Detailed scan*: For a single sample, to obtained detailed SAXS data at the bone-cartilage interface (BCI)
181 region, a square 2D area scan of 0.4mmx0.4mm at the interface was performed with 5µm increments in
182 the x and y-direction.
183 *Full-length scan*: For a single sample, to obtain the SAXS data for the full-scale length of the extracted
184 BCU core shown in **Figure 1C** (extending from AC through the full length of TB), a rectangular 2D
185 area scan of 5mm (vertical (y); distance from joint surface) × 0.38mm (horizontal (x); distance parallel
186 to joint surface) was performed, with 20 µm increments in both x and y-direction.
187 **Data Processing**:
188 SAXS analysis was carried out via a combination of DAWN (www.dawnsci.org), an Eclipse-based
189 software framework developed at Diamond Light Source[33], with customized model fitting routines
190 (in Python; Anaconda Python distribution from Continuum) applied to the 1D integrated intensity files
191 generated by DAWN. Fibril-level ultrastructural parameters (fibrillar D-period, fibrillar orientation and
192 degree of fibrillar alignment) were extracted from SAXS patterns, via both prior published protocols
193 developed in our group [9,18], and by use of new (non-parametric) methods of intensity peak centre
194 and width estimation.
195 *DAWN Data Reduction*: The 2D-rastered maps of 2D SAXS data (1 per array point) for each scan
196 (shown in **Figure 1D**), were reduced to 2D arrays of 1D intensity profiles. The radial $I(q)$ and azimuthal
197 (angular) $I(\chi)$ files were extracted as a function of scattering vector (q) or azimuthal angle (χ) depending
198 on integration mode (azimuthal and radial, respectively) shown in **Figure 1E**, and saved as text files.
199 The *Processing* perspective in DAWN was used for the batch reduction of the data files [33]. As well
200 as a mask file specific for the Pilatus detector, which excluded the dead-regions (seen as white strips in
201 **Figure 1D**) between charge-coupled device (CCD) plates or the beam-stop.

202 *I(q) processing for Fibril D-period*: **Figure 1G** shows an *I(q)* plot from our data with DAWN showing
203 the radial meridional peaks, particularly clear at the 3rd and 5th order diffraction peaks (wavevector range
204 0.1 to 1.2 nm^{-1}). For collagen-specific analysis, the 3rd order meridional peak was used because it is
205 clearly visible in both (uncalcified) cartilage, the calcified plate and in trabecular bone (in contrast to
206 the 5th order peak which is clearly visible in articular cartilage [9] but less clear in calcified tissue). After
207 azimuthal integration on DAWN, the *I(q)* data sets produced for each scan point were read by custom
208 Python scripts to perform the peak analysis for the desired parameters, as described below:
209 *1) Total SAXS intensity*: The total SAXS intensity was calculated from the area under the $I(q)$ curve.
210 Total SAXS intensity, primarily from diffuse scattering, is related to the amount of interfacial area
211 between nanoscale inclusions like mineral platelets and surrounding matrix in bone [34], or between
212 fibrils and the extrafibrillar matrix. Here, we use it to a) distinguish between the bone-cartilage core and
213 surrounding fluid and b) to distinguish between the calcified and uncalcified tissue regions in the scan,
214 as calcified tissue regions have much higher diffuse SAXS intensity arising from the mineral phase.
215 *2) Collagen peak intensity*: The collagen peak intensity is defined as the total area under the 3rd order
216 meridional collagen peak after diffuse background SAXS subtraction. Diffuse SAXS background
217 subtraction is done as per our previous protocols [9,35], by a linear interpolation of the diffuse signal
218 from the left (q = 0.27 nm^{-1}) to the right (q = 0.3 nm^{-1}) of the 3rd order meridional peak. The collagen
219 peak intensity is related to a) the total amount of collagen fibrils/unit volume present in the scattering
220 volume b) the degree of intrafibrillar order [18] and c) the orientation of the fibril in 3D space [36].
221 *3) Fibril D-period:* The fibril D-period arises from the axial periodicity in electron density along the
222 collagen fibril due to the gap-overlap stacking of tropocollagen molecules inside the fibril[37]. Shifts
223 in the D-period can be linked to axial fibril strain (e.g. [18,38–40]), and in cartilage, changes in the D-
224 period have been interpreted as changes in tensile pre-strain due to variations in swelling and osmotic
225 pressures in the proteoglycan-rich extrafibrillar phase [9,18]. For all points in the 2D scan, we set a
226 threshold of 0.025 (arbitrary units) in collagen peak intensity (from 2) above), above which the D-period
227 (and associated peak parameters) was estimated. The need for the threshold is because estimating the
228 fibril D-period is only meaningful where there are sufficient collagen fibrils at a point in the scattering
229 volume satisfying the Ewald diffraction condition and generating a clear 3rd order meridional peak.

To estimate D-period, initially a parametric peak fitting approach (starting with Gaussians) was used, following prior work in our group [9,41] and using the *lmfit* nonlinear least squares fitting package in Python [42]. However, we found that there was a pronounced rightward asymmetry in the peak profile, which was not visible in prior work [9,41]. The possible structural reasons for this effect (arising from fibre diffraction), and its implications for the measured D-period will be explored and justified in detail in the **Discussion**. Here, we note only that the peak asymmetry is visible due to the recent upgrade of X-ray optics at the I22 beamline (in 2019) which led to much higher resolution in the peak profile which could not be resolved in earlier work [9,18]. Due to the asymmetric peak nature, we use a nonparametric method-of-moments approach, treating the *I(q)* profiles (with the diffuse linear background intensity subtracted) as continuous distributions around the central wave vector (q) values, to find the parameters centre(μ) and sigma(σ). The first moment ($q_{FM}=\mu$), that is the expectation value μ, gave the position of the peak (q_0 in our prior notation[9]) and the standard deviation gave σ (the width of the peak). The following equations were used to calculate the first moment, the second moment and the standard deviation.

$$\text{First moment } q_0 \text{ or } q_{FM} = \frac{\sum q I_b(q)}{\sum I_b(q)} \qquad \textbf{Equation 1}$$

$$\text{Second moment, } q^2_{SM} = \frac{\sum q^2 I_b(q)}{\sum I_b(q)} \qquad \textbf{Equation 2}$$

$$\text{Standard deviation, } \sigma = \sqrt{q^2{}_{SM} - q_{FM}{}^2} \qquad \textbf{Equation 3}$$

where q and $I_b(q)$ are the wave vector and (background corrected) radial intensity values around the 3rd order peak, as shown in **Figure 1G**. From q_0 the D-period was calculated as (where n is the peak order, n=3 for the 3rd order meridional peak):

$$D = n\frac{2\pi}{q_0} \qquad \textbf{Equation 4}$$

To represent the SAXS scans as 2D images, parameters (like D-period, total SAXS intensity and collagen peak intensity) were displayed as a colour-scale bit-map, where the colour value was related to the value of the calculated parameters through a colour-map.

I(χ) processing for fibril orientation and degree of fibrillar alignment: 1D azimuthal intensity profiles I(χ) at each scan point were generated to obtain parameters characterising the angular collagen fibril distribution – the average fibril orientation χ_0, and degree of fibrillar alignment (ρ: random order→ρ=0, uniaxial alignment → ρ large). In a similar manner to the *I(q)* analysis, the background diffuse scattering needs to be corrected for. A three-ring subtraction method was used to obtain corrected intensity value, by radially averaging the intensity just outside of the peak and subtracting this average from the radial average on the peak, as described previously by us [43]:

$$\text{Collagen Intensity} = \text{Peak intensity} - \tfrac{1}{2}\,(\text{inner intensity} + \text{outer intensity}) \quad \textbf{Equation 5}$$

It is noted that across the full azimuthal 0-360° range, some parts of the detector were blocked due to dead-regions between Si pixel modules or the beam-stop. A restricted range from 0 to 180° where such blockages were minimized was therefore used. This restricted angular range provides the full information due to the theoretical χ→χ+180° symmetry of the scattering for SAXS (from to the Ewald sphere being approximated as a plane). The corrected intensity peaks, $I_{corrected}$ (after background subtraction in **Equation 5**) were fitted with a Gaussian model with zero baseline using a custom Python program using the *lmfit* nonlinear fitting package [42], as shown in **Figure 1H** and following our prior work [9,43,44].

The ρ-parameter was calculated from $I_{corrected}$ data by evaluating the Gaussian model fit results, using the following equation

$$\rho = (I_{corrected_max} - I_{corrected_min}) / I_{corrected_mean} \quad \textbf{Equation 6}$$

where $I_{corrected_max}$ and $I_{corrected_min}$ are the maximum and minimum values in the fit for $I_{corrected}$. Note this parameter (for unmineralized and mineralized collagen) is quantitatively different from the Rho-parameter used earlier by Fratzl and colleagues [45] for mineralized tissues, (though qualitatively both are measures of the degree of alignment of the fibril) and is hence denoted with the symbol ρ.

A custom Python script using the *matplotlib* package[46] was used to display the colour map of the calculated orientation parameters, where the angle of the line shows the fibrillar orientation. Both the length of the line, and the colour value of each pixel corresponds to the degree of fibrillar alignment (ρ), similar to prior work [10]. The definition of degree of fibrillar alignment ρ used here differs from the rho-parameter used earlier for degree of mineral particle alignment in bone [45], but has qualitative similarities in that both are used to represent angular anisotropy of nanoparticle/nanofibre alignment and are close to zero for randomly oriented nanoscale inclusions.

Zonal assignment: To analyse differences in these SAXS parameters across tissue zones, we first used scalar measures from the SAXS pattern to classify a point as belonging to 1) articular cartilage (AC), 2) calcified plate (CP), or trabecular bone (TB). Within articular cartilage, we further subcategorized points as arising from the superficial, transitional, or deep zone. First, a threshold of 2.0 [arbitrary units] in total SAXS intensity was used to differentiate between articular cartilage (low total SAXS intensity) and calcified plate (high total SAXS intensity due to mineral scattering). The dense cortical calcified plate and the spongy trabecular bone regions were differentiated based on the vertical *y*-coordinate, as the cylindrical sample geometry leads to a simplified 1D (vertical *y*) variation in the sample tissue structure, and a visually clear demarcation between the calcified plate and the trabecular bone. For zones within in the articular cartilage region, the *degree of fibrillar alignment* ρ and *direction of fibril orientation* χ_0 were used as differentiators: points with low ρ (< 2.1) with randomly aligned fibrils were assigned to the transitional zone (TZ). Points above the transitional zone and with χ_0 around 0° or 180° (horizontal) was assigned to the superficial zone (SZ), and points below with χ_0 around 90° were assigned to the deep zone (DZ). The justification for this assignment is the well-known arcade-like

Benninghof structure [7] for the fibril orientation in articular cartilage. For all samples, a 5-color map (SZ/TZ/DZ/CP/TB) of the scans was generated, based on these assignmens, and visually inspected to check that this classification did not result in any artefacts, e.g. an assignment of a point deep inside the trabecular bone to the calcified plate category; all 5-color maps for regions are also shown in **Supplementary Figure 1.**

Data analysis, fitting and statistical analysis: To compare the SAXS-derived parameters between tissue zones, two parallel approaches were used: 1) a *zonally-averaged approach* across-samples and 2) an *intra-sample* approach.

For 1), the mean value of each SAXS-parameter was calculated for each zone and each sample (n=6 samples). To account for the inter-sample variability, we used a paired t-test (two-tailed) protocol to compare the SAXS-parameters between adjacent zones (SZ-TZ, TZ-DZ, DZ-CP and CP-TB).

In the complementary approach 2), for each sample-scan, every SAXS pattern in the scan was assigned to zones SZ, TZ, DZ, CP or TB based on the protocol described above, and reduced to obtain the relevant SAXS parameters. Statistical comparison of each SAXS-parameter was carried out by 1-way ANOVA, with the zone as the variable. After Anova, Tukey's honestly significant difference (HSD) pair-wise tests were carried out between data in different zones. Statistical test-results were reported on a per-sample basis and histograms of the SAXS parameters were also plotted.

The approach 1) of paired t-test analysis is reported in the main text, and the intra-sample approach 2) in the Supplementary Data. This is because the main scientific question is whether there are (on average) differences in SAXS-derived ultrastrucutural parameters across zones in the bone-cartilage unit.

The paired t-tests were carried out in Microsoft Excel and the 1-way analysis using R (www.r-project.org). For data fitting, custom Python scripts (Anaconda Individual Edition;

www.anaconda.com) using the packages *lmfit* [42]and *matplotlib* [46] were used for the analysis of $I(q)$ and $I(\chi)$ profiles created in DAWN, along with Microsoft Excel.

Results

Spatial gradients of fibrillar-parameters across the BCU:

In the following, we present quantitative 2D mapping and zonal analysis of ultrastructural SAXS-based parameters across the bone-cartilage unit at different length-scales. **Figure 2A** shows the classification of the different tissue regions into five zones: in articular cartilage, the superficial (SZ), transitional (TZ) and deep (DZ) zones, and in the calcified tissue, the dense calcified plate (CP: a mix of calcified cartilage and subchondral bone) and the trabecular bone (TB). **Figure 2B-D** shows 2D maps of the micro-spatially varying nanostructural parameters derived from $I(q)$ (D-periodicity, total SAXS intensity and collagen peak intensity) across the BCU. The D-period exhibits two clear features: i) a gradient of increasing D-period from the surface of the joint to the deep zone in articular cartilage, which is maintained in the calcified plate, followed by ii) a distinctly lower D-period range across the underlying trabecular bone (where no spatial gradient is seen). It is noted that the D-period in the calcified plate is higher than the trabecular bone despite both being comprised of mineralized collagen. **Figure 2C** also shows that the total SAXS intensity *a)* is low in articular cartilage, *b)* shows a clear high band in the calcified plate, due to strong SAXS scattering contrast from the mineral relative to the surrounding organic phase, and *c)* exhibits a patchy cellular structure in the TB, reflective of the porous mineralized tissue structure in trabecular bone.

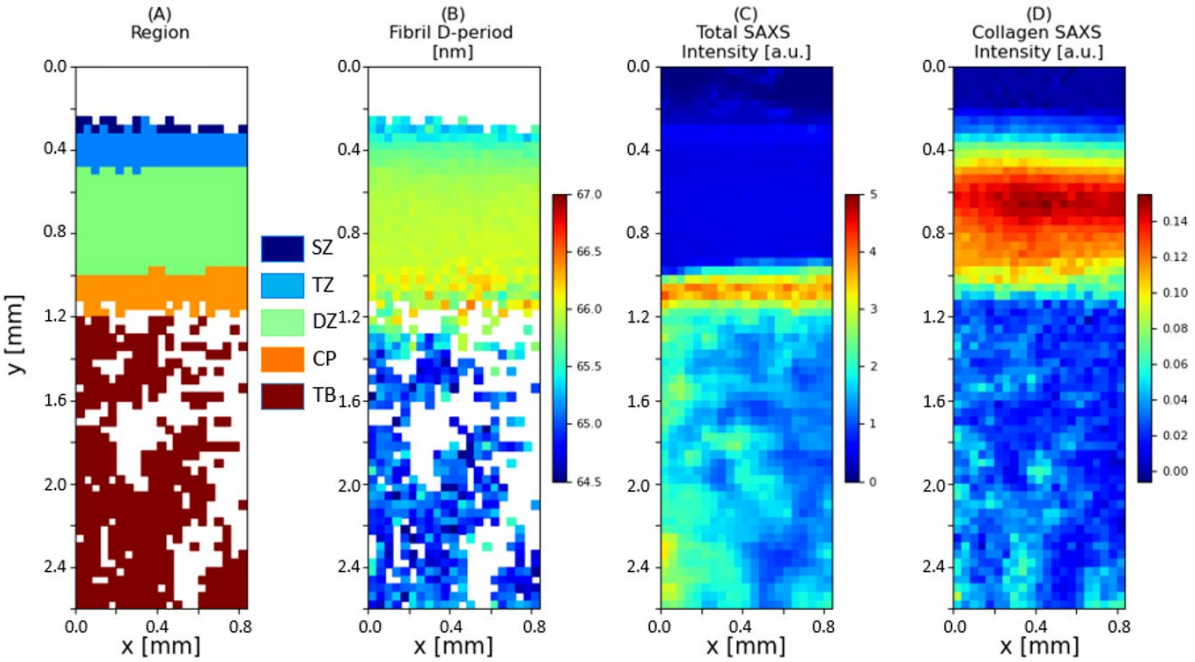

Figure 2: *Variation of fibril pre-strain and ultrastructural SAXS measures across the BCU*: Colour plots of 2D SAXS scan on a bone-cartilage unit (BCU) (A) Region, with the acronyms following the region classification in **Figure 1A**, (B) Fibrillar D-period (nm), (C) Total SAXS intensity (a.u.) and (D) Total diffraction intensity from the background-corrected meridional collagen peak intensity (a.u.). The plots show the variation in these nano structural parameters across the BCU.

In a complementary manner, for the fibril orientation derived from I(χ), **Figure 3** shows the 2D parameter map for the orientation direction and extent of orientation ρ for the same sample shown in **Figure 2**. The orientation follows the well-established Benninghof ultrastructure of fibres, with superficial-zone fibrils aligning along the horizontal plane (around 0°/180° angle), no preferred direction in the transitional zone (short lines within each voxel), fibrils in the deep zone and calcified plate aligning vertically (around 90° angle) and no preferred direction in trabecular bone (short lines). The superficial zone, characterised by fibrils oriented parallel to the joint surface, is most easily identified by fibre direction coupled with a higher degree of alignment ρ than in the adjacent transitional zone. The colour scale (representing ρ) shows higher ρ values in the deep zone and the calcified plate as compared to transitional zone and trabecular bone.

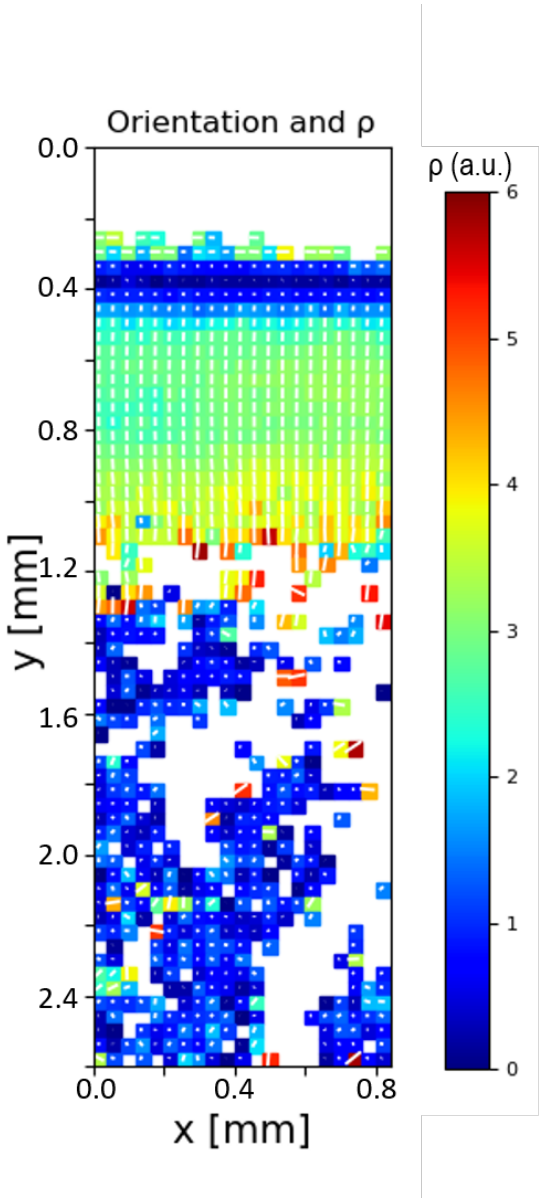

Figure 3: *Fibril orientation and alignment across the BCU*: Colour map (for the sample in **Figure 2**) for collagen fibril orientation (degrees) and ρ (a.u.) parameter, where the length of the white line and the colour scale corresponds to ρ, and the direction of the white line indicates the fibrillar orientation across BCU. There is a clear increase in the degree of fibrillar alignment at the BCI, with the fibrillar orientation perpendicular to articulating surface. However, there is random orientation with lower degree of alignment in TB.

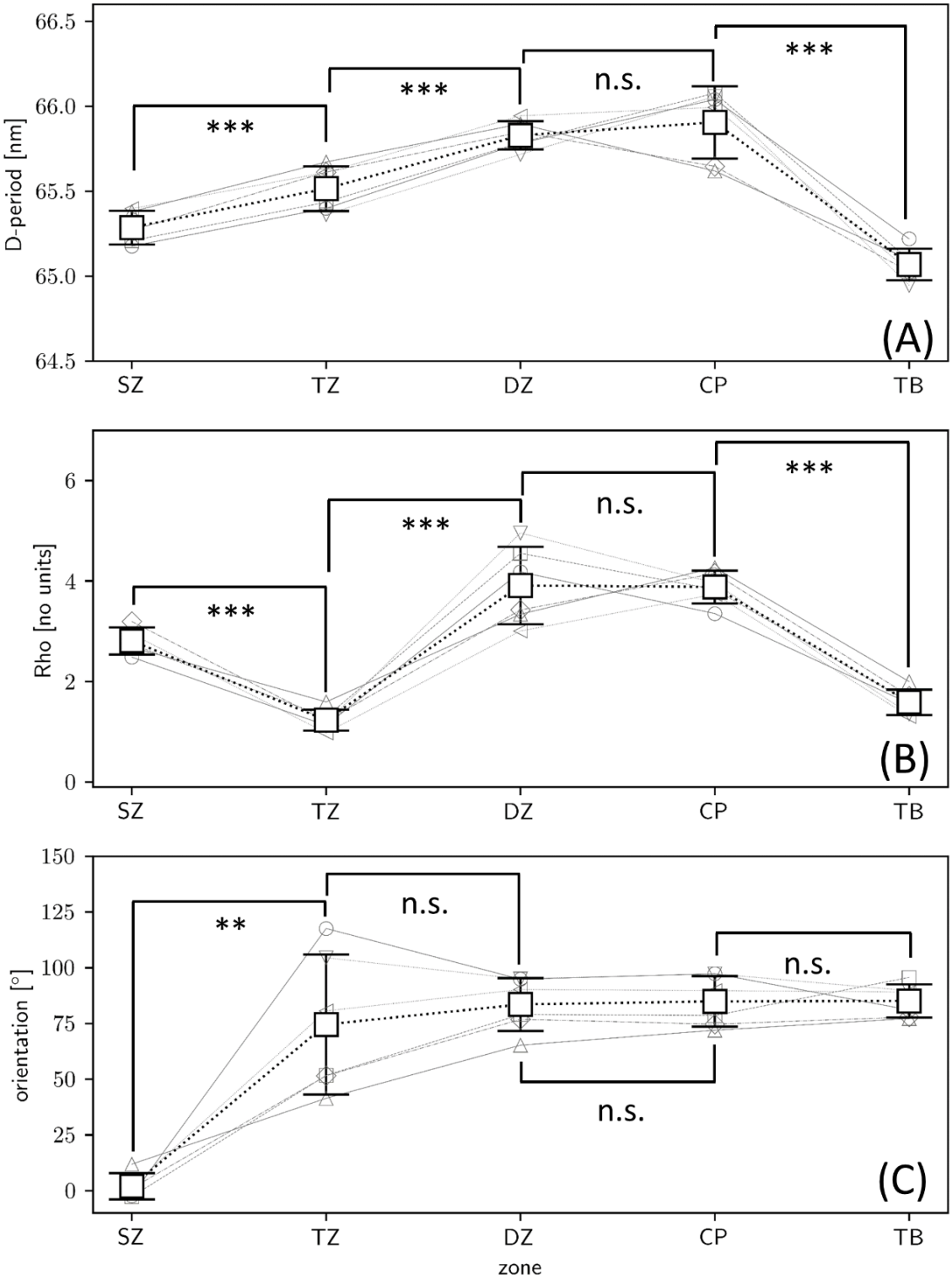

Figure 4: *Significant difference in fibrillar pre-strain, alignment, and orientation across the BCU*: Bar plots of the (A) fibril D-period (pre-strain), (B) degree of alignment (ρ) and (C) fibril orientation direction. The SAXS ultrastructural measures are calculated on a per-zone basis for each sample (small symbols, grey outline), which are averaged across the regular scan (n=6) samples and shown as white squares; error bars: standard deviation across samples.

386 **Significant differences in fibrillar-parameters between zones:**

387 To extract the mean values of the SAXS-derived parameters, and estimate statistical differences
388 between zones, first histograms are plotted on a per-zone basis (**Supplementary Figure 2**). Mean
389 values and standard deviations are calculated per zone. To compare the differences in mean values, on
390 a per-sample basis, **Figure 4** reports the result of paired *t*-tests between adjacent tissue zones. The D-
391 period increases significantly on going from the superficial to the transitional zone, and from the
392 transitional to the deep zone. The differences between the deep zone and the calcified plate are not
393 significant, but a highly significant reduction is observed in D-period between the calcified plate and
394 the trabecular bone. For the degree of orientation ρ, significant reductions occur on going between the
395 superficial and transitional zone, and significant increases between the transitional and deep zone. Like
396 the D-period, ρ is not significantly different between the deep zone and calcified plate but is much lower
397 in the trabecular bone versus the calcified plate. As described in *Materials and Methods*, as an alternate
398 analysis method (2), we carried out 1-way ANOVA tests on a per-sample basis (contrasting with the
399 paired approach comparing per-sample means here), giving similar results (**Supplementary Table 2**).
400

401 **Qualitative differences in meridional SAXS peak profile between zones:**

402 Since the zonal variation in D-period is small (e.g., ~65.2 nm to 66.0 nm in **Figure 4**) as is often the
403 case in collagenous tissues [18,47], it is a reasonable question as to how significant these changes are,
404 and whether our new non-parametric method of peak estimation may be artefactually influencing the
405 difference. First, we note that the magnitude of the effect (~1%) is comparable to the fibril-level strains
406 experience in bone under deformation to fracture [43]. To further clarify this, we plot $I(q)$ profiles, with
407 and without diffuse SAXS background subtraction, from each of the 5 different zones in an example
408 BCU (**Figure 7**) to see how evident these peak-profile differences are in the original data itself. It is
409 clear, especially from the background subtracted data (**Figure 7B**), that there are distinct changes in
410 peak position and shape across the zones; most notably, the right-shifted $I(q)$ for TB demonstrates the
411 lowered D-period seen in the colour-plots in **Figure 2** and **4** and quantified in **Figures 3** and **5**. **Figure**
412 **7B** also shows that in AC, the total SAXS intensity due to the collagen peak alone (excluding the diffuse

SAXS scattering) is maximum in the DZ, and least in the SZ. This effect may arise due to a combination of varying collagen concentration as well as degree of fibrillar ordering (higher ordering corresponds to higher SAXS peak intensity [9,47]). Interestingly, the collagen peak height is also larger in CP than in the TB region.

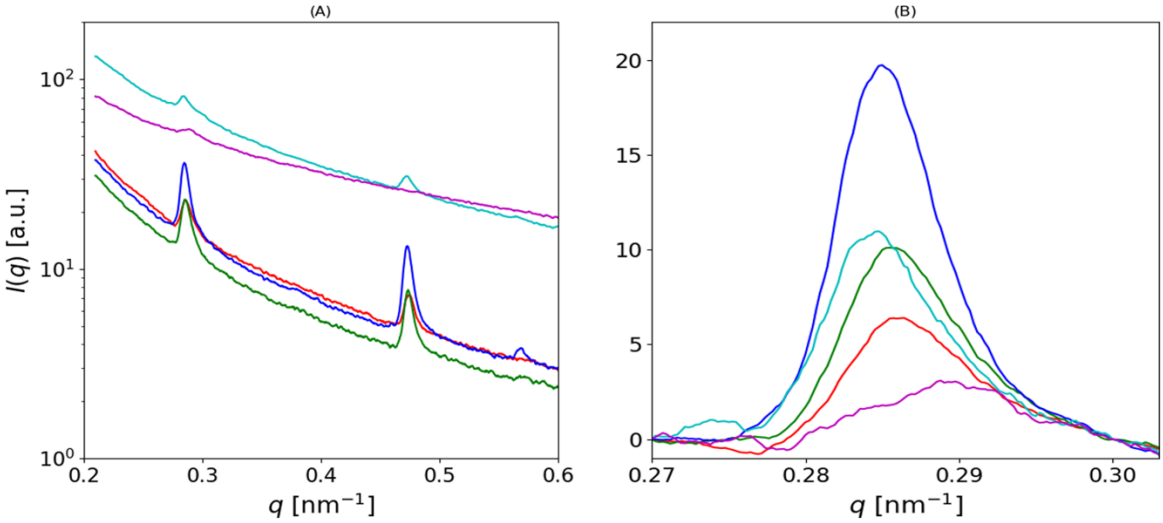

Figure 5: *Variation of SAXS intensity profiles across zones:* (A) I(q) plot, showing 3rd order and 5th order peaks due to collagen D-period, after azimuthally integration around the diffraction pattern for the q-radial range 0.2-0.6nm^{-1}. (Red: SZ, Green: TZ, Blue: DZ, Cyan: CP and Magenta: TB). (B) The 3rd order collagen peaks across the BCU after the diffuse SAXS background subtraction.

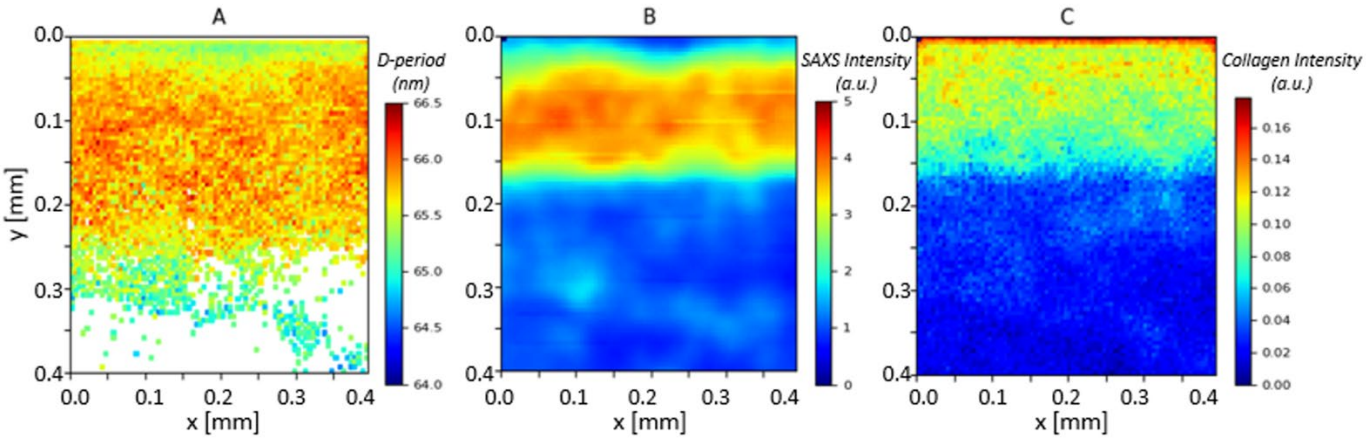

Figure 6: *High spatial resolution map of fibril pre-strain and ultrastructural SAXS measures at the calcified/uncalcified boundary in the BCU*: (A) D-period, (B) SAXS total intensity and (C) SAXS collagen intensity. The uncalcified articular cartilage is at the top of the image (blue shaded region near the ordinate value of 0.0mm for B); the calcified plate (CP) is from ordinal values of 0.0-0.2mm (yellow-red regions in B), and the regions from 0.2mm and below are the trabecular bone (TB) region. In A), the D-period shows a lower average value near the interface. SAXS collagen intensity is higher toward the interface.

High resolution SAXS mapping at the interface shows finer-scale gradients:

To map out the ultrastructural variation of the fibril parameters at the calcified interface itself, **Figure 6-7** shows the high-resolution colour maps with 5 μm spacing. Laterally-averaged line-profiles of the same data are shown in **Figure 8**, to more clearly shown the spatial variation with distance from the articular cartilage/calcified plate interface. The location at the top of the images corresponds to the transition from unmineralized deep zone articular cartilage to the calcified plate, evidenced by the lower total SAXS intensity coupled with the high collagen peak intensity. As indicated by the arrows in **Figure 8A**, over a region of about 70 μm, the D-period is observed to increase from ~65.4 nm to 65.8 nm (~0.6% increase) (**dashed line a1**), following which the D-period is approximately constant over ~70 μm (**dashed line a2**). The D-period then exhibits a decrease over ~170 μm to ~65 nm (**dashed line a3**), following which the trend stabilises, which corresponds to reaching the trabecular bone region.

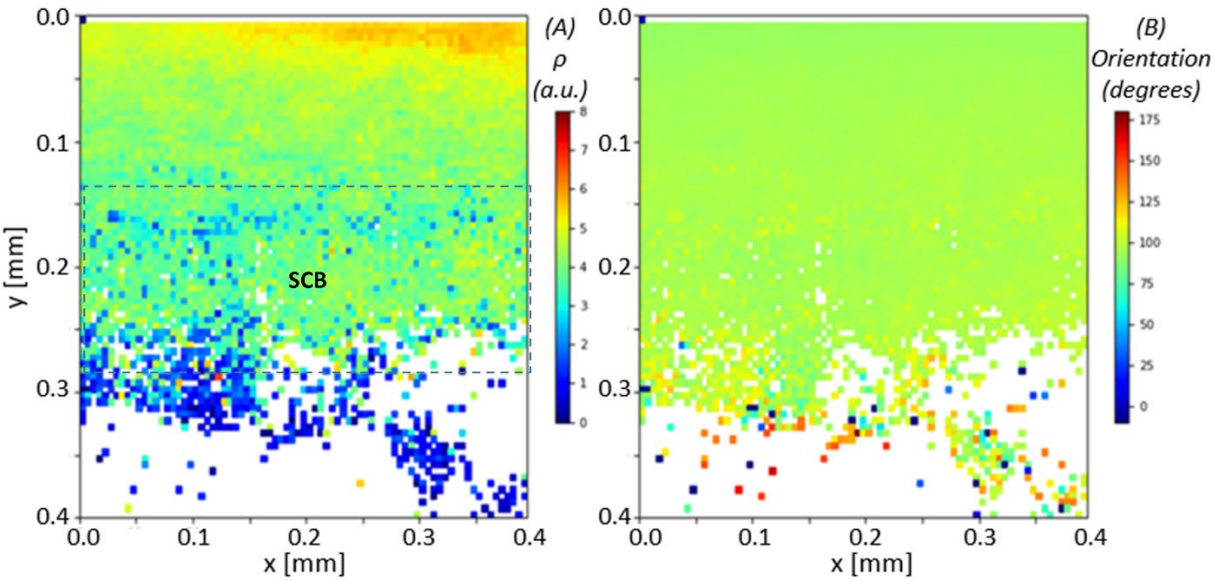

Figure 7: *High spatial resolution map of fibril degree of alignment and orientation at the calcified/uncalcified boundary in the BCU* (same sample as in **Figure 6**) (A) degree of alignment ρ and (B) collagen fibril orientation. From A) the tissue shows a high degree of fibrillar alignment when transitioning from the deep zone of articular cartilage to the calcified plate, and in B) we see fibres predominantly orientated in the angle of 90° (green colour), perpendicular to the articulating surface. In the lower part of the calcified plate (dashed rectangle; ordinal values from 0.15mm to 0.3mm) the ρ values are lower than in the upper part; it is suggested this is subchondral bone as opposed to calcified cartilage. From 0.3 mm downward, the degree of orientation is much lower, and orientation is more random, characteristic of trabecular bone.

Interestingly, on comparing **Figure 8A-B**, the D-period variations show different correlations with the degree of fibrillar alignment ρ, depending on where one looks in the BCI. For the transition from AC to CP (on the left in **Figure 8A-B**), the increase in D-period is accompanied by a decrease in ρ by about 20% (**dashed lines a1 and b1**). On the right-hand side in **Figure 8A-B** (also indicated by the region "SCB" in **Figure 7**), there is a transition to lower ρ (**dashed line b3**), followed by further decline as the TB region is approached (**dashed line b4**). In contrast to the AC/CP transition behaviour, on the right-hand side (CP/TB transition), the D-period decreases with reduction in ρ (**dash lines a3 and b3**). On the left-hand side in **Figure 8C**, orientation of the fibrils is predominantly perpendicular to the AC/CP interface ($\chi_0 = 90°$), which is a well-known "anchoring" type of architecture for the uncalcified AC to adhere to the SCB. The variance in orientation is less toward AC/CP interface (evidenced by a more homogeneous colour distribution as shown in **Figure 7B**). On moving toward the TB-region, we see a trend to wider ranges of fibril orientations χ_0, coupled with overall lower degree of alignment ρ, which is low in TB.

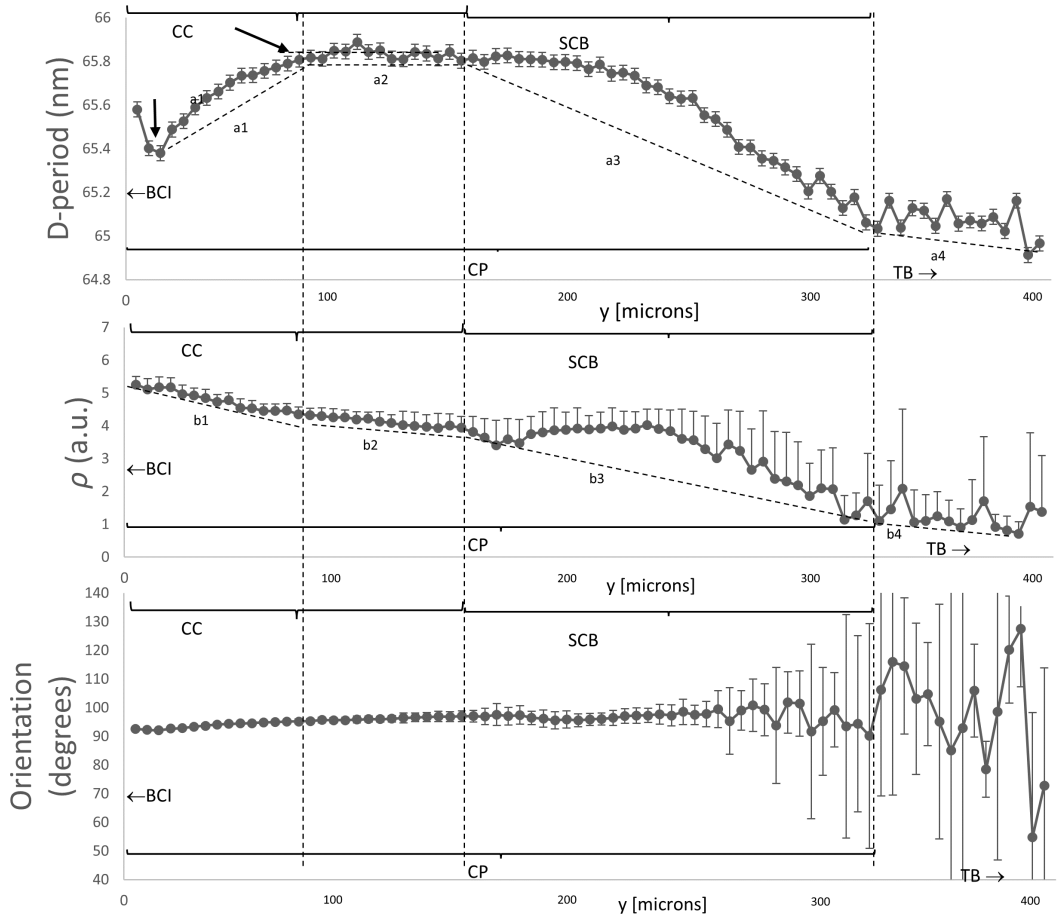

Figure 8: *Variation of fibril D-period, degree of orientation and direction of orientation across the bone-cartilage interface*: 1D line plots, averaged in the horizontal direction, for the high resolution 2D scans in **Figures 6-7**. (A) The mean D-period (B) mean ρ and (C) mean orientation, averaged for each y-coordinate, displayed with error bars representing standard error of the mean. Horizontal (abscissa)-axis is in microns. Interface between calcified and uncalcified cartilage is on the left, indicated by BCI with left-arrow. In A), it is noted that D-period rises from a local minimum toward the interface between the calcified plate and articular cartilage (on the left); it stabilises at the first vertical dashed line ~100 μm to the right of the interface. The right two vertical dashed lines indicate a proposed demarcation of the calcified plate (CP) into calcified cartilage (CC) and subchondral bone (SCB), at the same points as the dashed rectangle in **Figure 7A**.

Discussion

In summary, the main new findings in this paper are:

- Existence of a variation in fibrillar D-period (linked to fibril pre-strain), extending across the uncalcified articular cartilage (shown by us before [9]) which stabilizes between the deep zone and the underlying calcified plate, i.e. across the bone-cartilage interface.

- A reduction of the D-period in the underlying trabecular bone to the values characteristic for Type I mineralized collagen.
- A finer-scale modulation of this gradient at the deep-zone/calcified plate interface, with high-resolution scans showing a short-length scale (~80 μm) drop and increase in D-period.
- Highly significant differences in D-period and in the degree of alignment ρ across all zones except between the adjacent deep zone and calcified plate.
- Evidence of two distinct regions with altered nanostructure inside the CP, from both fibrillar alignment and pre-strain.

The increased fibril D-period in the calcified plate is surprising, when considering the well-established fact [28,48] that the D-period for mineralized collagen in bone (for example) is consistently lower than hydrated unmineralized collagen. Mineralisation inside and around the fibrils has been linked to dehydration of collagen [26,27], which leads to a lower D-period (~65 nm). The reasons for the reduction could include axial shrinkage [26] or a change in molecular tilt [24]. However, biochemical differences between Type I (bone) and II collagen (calcified cartilage) may couple with altered intra- and interfibrillar mineralisation patterns in calcified cartilage leading to a larger D-period. In contrast, the D-period of ~65 nm for trabecular bone is consistent with previous studies of Type I mineralized collagen [16]. It is noted that calling the changes in D-period as changes in pre-strain is an approximation, since it assumes that the fibrils have similar zero-stress D-periods (or reference states) across the tissue types (articular cartilage, calcified plate and trabecular bone). Further, the change in pre-strain may be associated with alterations in molecular level tilt [22,24] or ordering of tropocollagen molecules in the fibril [18], which are intrafibrillar mechanisms we do not consider here.

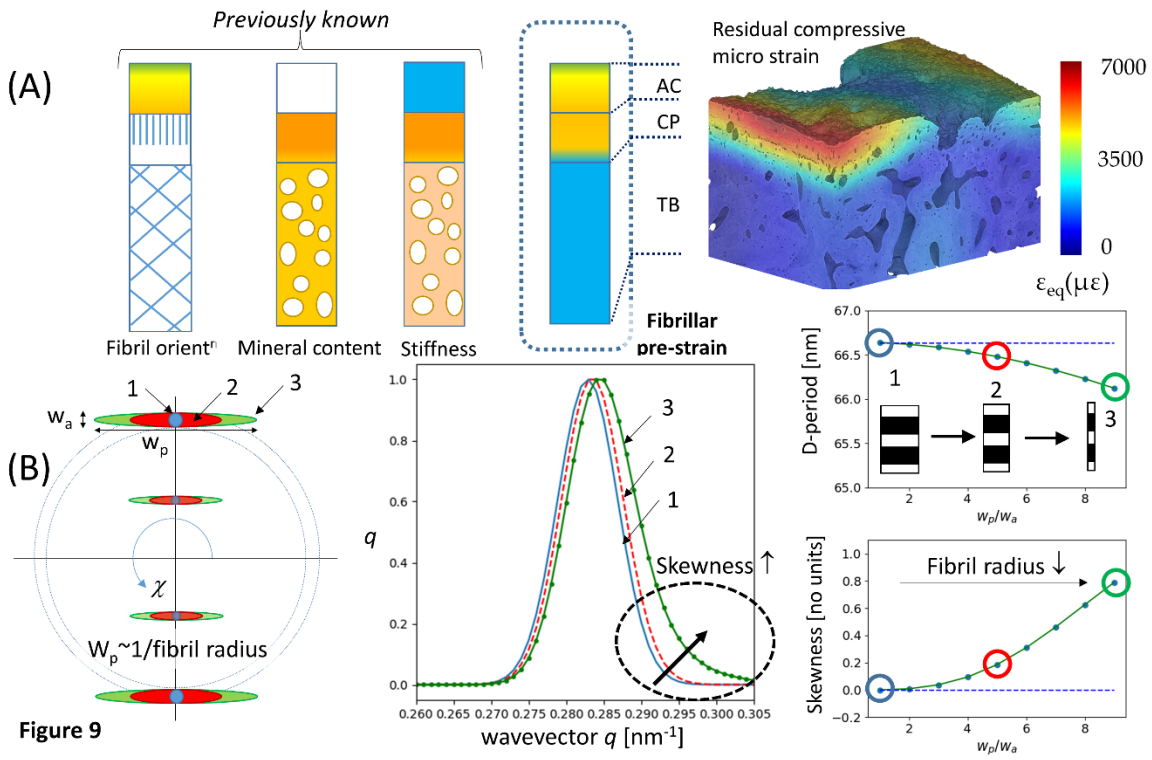

Figure 9

Figure 9: *Schematic overview and X-ray fibrillar model:* (A) Correlation between nanoscale fibrillar pre-strain and microscale residual compressive strain. Left: schematic of fibrillar pre-strain gradients (this work; **Figs 2**, **3** and **6**) across the AC, CP, and TB in the bovine metacarpophalangeal joint. Right: From independent work on the bovine patellar joint [49], residual compressive strain (after loading) visualised using microcomputed tomography (CT) digital volume correlation (DVC). The calcified plate (both CC and SCB) are seen as regions with both high fibrillar tensile pre-strain (in unloaded state) and high compressive strain (energy storage) after loading.(B) Fibre-diffraction simulations showing how increasing fibril radius affects the skewness of the peak and estimated D-period. *Left*: schematic of meridional SAXS ellipsoidal peaks from a single fibril for different ratios of parallel to axial peak widths w_p/w_a. Blue: w_p/w_a = 1; red: w_p/w_a = 5; green: w_p/w_a = 10. *Middle*: Simulated I(q) plots for 3rd order meridional peak for these ratios (with D-period kept constant), showing increasing skewness as w_p/w_a increases, along with a slight rightward peak shift. *Right*: effect of increasing w_p/w_a from 1 to 10 on (top): D-period calculated by moments method and (bottom) peak skewness, showing that the moment method underestimates the D-period as fibril radius decreases (1→2→3).

The higher resolution of the SAXS configuration compared to previous configurations [9,18] means some features like the peak asymmetry are visible where before they were hidden by beam divergence. We believe the finite fibre diameter is influencing this asymmetry via a fibre-diffraction effect [50], conceptually sketched in **Figure 9B**. Fibrils with axial electron-density periodicity of D and radii R exhibit a set of parallel ellipsoidal layer-line reflections (spacing 2π/D), with finite width (w_p: p: parallel) proportional to 1/R perpendicular to the fibril axis [50]. Thinner fibrils will have greater w_p (e.g. case 3 (thin fibril) vs case 1 (thick fibril) in **Figure 9B**); the axial width w_a is kept constant in this sketch. The polar azimuthal (circular) average of flat ellipsoids parallel to the q_x axis thus leads to a

531 rightward skew asymmetry of the integrated peak (simulated data shown in **Fig 9B**, centre), as the tails
532 of the ellipsoids contribute to larger wavevector values in the azimuthal (χ) integration. As a result, the
533 measured D-period (via weighted moments) underestimates the true D-period (as $q_3=6\pi/D$), with an
534 increasing skew correlated to a reduced measured D-period. **Figure 5B** shows that (especially in
535 cartilage) there is pronounced rightward skew of the I(q) peak. As a result, the estimated D-period via
536 our nonparametric method is likely an underestimate in these regions, and the pre-strain level in both
537 the AC- and CP-regions are even larger than estimated here, and the differences with respect to the
538 underlying trabecular bone maintained.
539
540 To confirm the above, we carried out a simulation-experimental test (**Supplementary Information:**
541 **Fibre Diffraction Modelling**), where the skew-effect was incorporated. Briefly, using fibre-diffraction
542 models of the type shown in **Figure 9**, model SAXS peak functions with varying levels of (fibre-
543 diameter induced) skew were generated for a range of axial and parallel peak widths w_a and w_p. By
544 matching the experimentally observable skew and axial width parameters for a representative sample,
545 the true D-period can be estimated (**Supplementary Figure 6**). It is seen that while the cartilaginous
546 tissue D-period is elevated in comparison to the first-moment method, the difference between the high
547 D-period in the cartilaginous tissue and the lower D-period in the underlying trabecular bone is
548 maintained. Future work will include concurrently fitting the azimuthal and radial intensity profiles, to
549 independently determine w_p as well as D, thus enabling a point-wise estimation of this effect. For the
550 current results, we note only that the difference between the D-period of the articular cartilage/calcified
551 plate (Type-II collagen fibrils) and the trabecular bone (Type-I collagen fibrils) is maintained.
552
553 The finer-structure gradient at the BCI interface, and the colour-contrasts in **Figures 6-7**, are intriguing
554 and we believe are linked to the two-phase calcified cartilage and cortical subchondral bone material
555 comprising the calcified plate. The length scale of ~70 μm over which the D-period rises from a local
556 minimum right at the DZ/CP interface is similar to previously reported thicknesses of the tidemark [10],
557 and suggests a compliant, less pre-strained region right at the interface. The more homogeneous fibrillar

alignment (ρ) in the upper half of the calcified plate in **Figure 7A** versus the more heterogeneous distribution further down suggests a division between calcified cartilage (toward the articular cartilage) and the subchondral bone (toward the trabecular bone). Assuming this assignment, our results demonstrate that the high degree of fibrillar alignment and uniform orientation in the calcified cartilage (as shown earlier [10,51,52]) is coupled with a rapid rise in fibril D-period which reaches ~65.8 nm (typical of uncalcified cartilage [9]) and remains constant for ~50 μm in the calcified cartilage and a further 50 microns in the subchondral bone, followed by a decrease over ~100 μm in the subchondral bone down to typical ~65 nm values in the trabecular bone.

We speculate that the increased tensile fibril-level pre-strain in the calcified plate (**Figure 2,3**) has a biomechanical function related to increased elastic energy storage under compression. In the calcified plate, stiff fibrils are oriented parallel to the compressive loading direction (as shown earlier, e.g. [10]) and in a state of tensile pre-strain relative to the fibrils in trabecular bone. On mechanical loading, under compression, the pre-stretched fibrils can compress down from the pre-strain level down to zero, before compressive failure mechanisms like buckling start becoming operative. This mechanism is supported by prior work on patellar joints showing large residual strains in the calcified interface measured by digital volume correlation [49], and is shown schematically in **Figure 9**. This schematic Figure shows how the zones of high nanoscale fibrillar pre-strain (from this work) in the calcified plate correlate closely with the high microscale residual compressive strains at the BCI after compressive loading (measured with digital volume correlation methods on tomographic (CT) images [49]). A limitation of this comparison is that the joint analysed in [49] is the bovine patella, whereas here we have tested the bovine metacarpophalangeal joint. Nevertheless, it can be speculated that this natural gradient in ultrastructural tissue properties may enable absorption (and release) of significant stored elastic energy in regular biomechanical loading, with a material energy density of $\frac{1}{2} E \varepsilon^2$ where E is the tissue elastic modulus of E~10-20 GPa [49], and ε the fibril pre-strain level of ~1.5%. Indeed, disruption of this ECM material-level energy absorption mechanism due to tidemark duplication in OA could be a biomarker-level indicator of OA progression.

585

586 Turning to the limitations of our work, a basic technical drawback is the use of 2D SAXS mapping of
587 what is intrinsically a 3D cylindrical tissue object. Nevertheless, we mitigate these effects by choosing
588 a cylindrical sample geometry, with relatively tissue homogeneity along the X-ray beam direction,
589 coupled with a limited lateral width across the scan versus the height (high aspect ratio). Further, the
590 variations we are interested in are along the length of the sample, rather than through the thickness, and
591 are thus relatively insensitive to such 3D effects. For full-scale 3D reconstruction of the depth-
592 dependent nanostructure, SAXS tensor tomography [36,53] will be essential. Secondly, we limit
593 ourselves to static scanning (no in situ mechanical loading) and leave spatial mapping of fibrillar
594 mechanics under loading to future work. Thirdly, we have limited our sampling to a specific condylar
595 anatomical site in the metacarpophalangeal joint and given that *in-vivo* strains vary across the joint, it
596 would be interesting to test if nanomechanical parameters like pre-strain shows a correlation with
597 varying physiological force levels across the joint. Lastly, we have not yet considered changes in OA
598 and ageing, to establish a baseline characterisation of the normal BCI in an animal model; a recent study
599 [11] has shown that nanoscale mineral particle thickness is significantly different in OA versus normal
600 human patients and investigating in situ mechanical response in aged human cartilage would no doubt
601 be of importance.

602

603 The use of scalar measures like SAXS intensity along with orientational information like fibrillar
604 alignment ρ and direction χ_0 enables us to classify tissue location based on properties of the oriented
605 collagenous ECM (as shown in **Figures 2A**). The method allows discrimination within the AC
606 (superficial, transitional, and deep zones) as well as between the AC, CP/SCB and TB regions. More
607 advanced machine-learning classification methods have been used on the diffuse SAXS signal enabling
608 distinction of the CP and SCB as well [11]; it would be of interest to apply such methods to the current
609 data in future analysis. The nonparametric method for peak estimation arises from the pronounced peak
610 asymmetry and the likely limits of linear background interpolation without a model. Recent analysis on
611 pericardium collagen using step-function scattering models may, similarly, point the way to a the better
612 analytical fitting of the peak profiles [54]. Nevertheless, the clear distinction between the meridional

peaks (particularly the peak positions of the TB viz the CP/SCB region) is visible in the raw data itself (**Figure 5**) and will likely not be affected by such further analyses.

In summary, we have demonstrated the existence of a multiscale gradient in the fibrillar pre-strain across the bone-cartilage interface in bovine joints, along with an elevated pre-strain mainly in the CC zone. The elevated pre-strain in the CP contrasts with the lower values in the underlying TB. Investigating the link between this nanoscale ECM structural change and the in-vivo biological growth dynamics would be interesting. Further, given that the BCI is subjected to considerable shear strains during loading [14], and disruptions to the interface have been implicated in OA progression [55,56], understanding how the ECM architecture of the interface is designed to resist physiological loading, and how it may be altered in injury, ageing and musculoskeletal degeneration would be worth investigating to both understand the process and as well as to define better structural biomarkers of joint degeneration.

Acknowledgements

HSG (BB/R003610/1, EP/V011235/1) and NJT (BB/R003610/1, EP/V011235/1) thank the BBSRC and EPSRC for research grant funding. HSG thanks MRC (MR/R025673/1) for funding. We thank Diamond Light Source (DLS) for the generous award of synchrotron beamtime (SM25602-2).

Supporting Information

Supporting Information is available from the Wiley Online Library or from the author.

- 6 Supplementary Figures
- 2 Supplementary Tables
- Supplementary Text

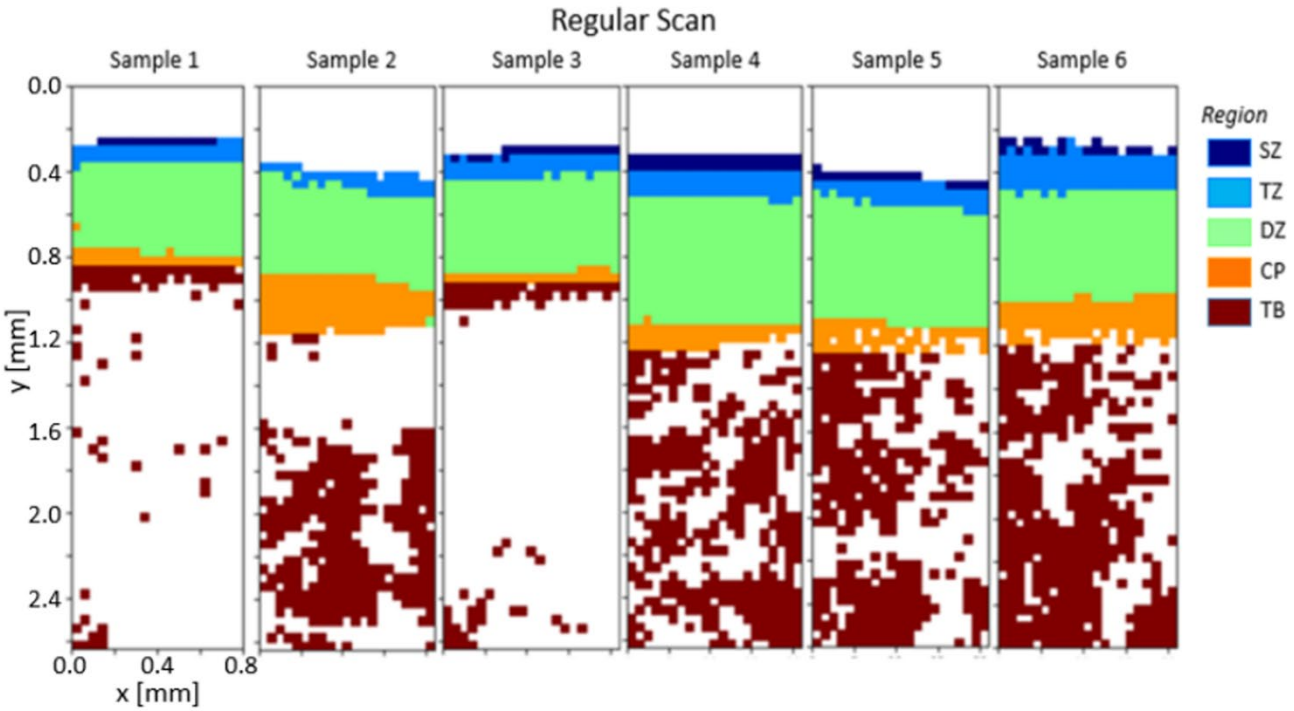

Supplementary Figure 1: Representation of the region classification into SZ, TZ, DZ, CP and TB, for the 6 samples used in the analysis. Note that Sample 2 does not have an observable superficial (SZ) zone. The colour indicates the type of tissue region across BCU.

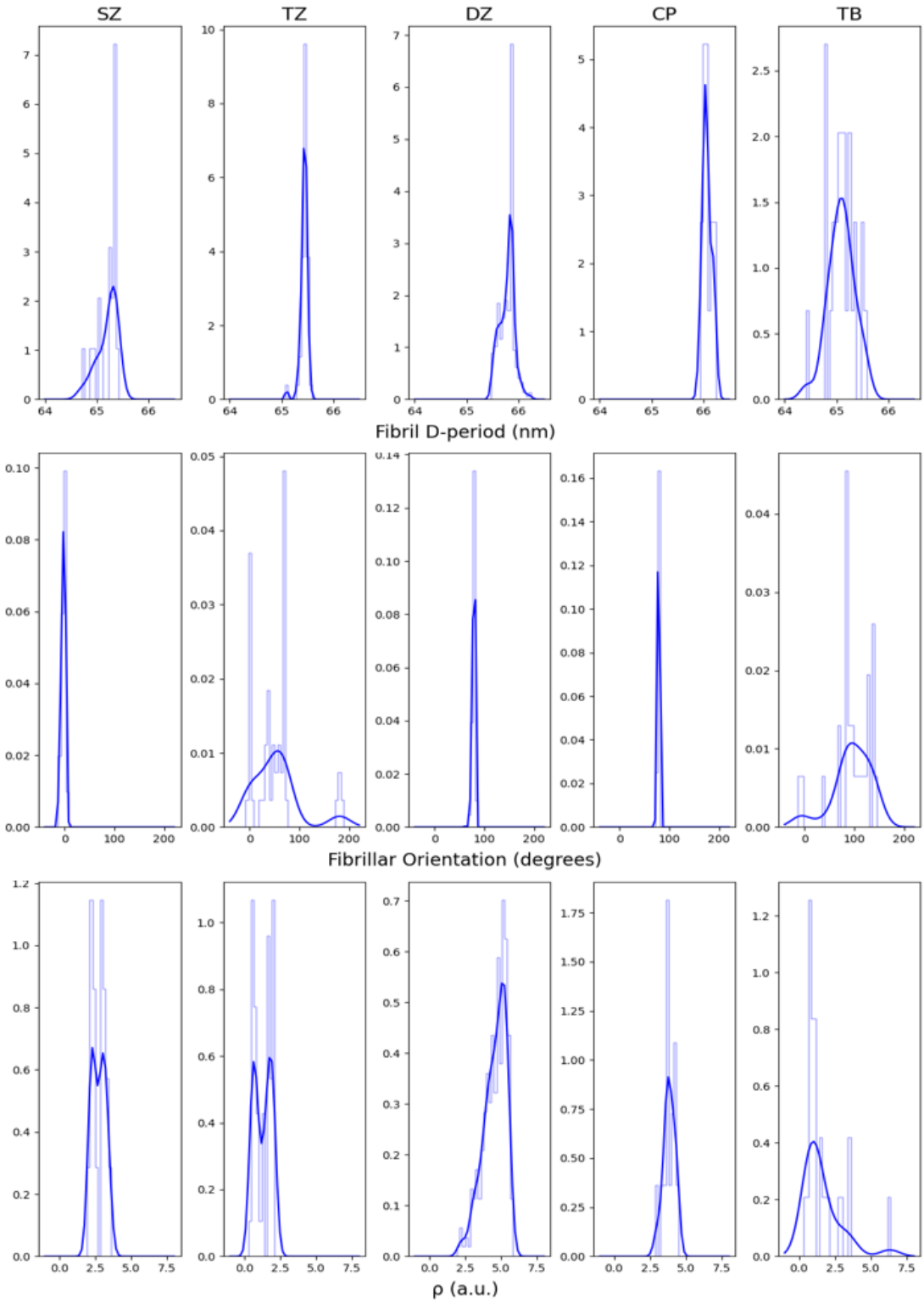

Supplementary Figure 2: *Top to bottom*: Histograms of the D-period, fibril orientation and ρ for the representative sample in **Figures 2-3**, for (left to right) the SZ, TZ, DZ, CP and TB tissue regions, respectively. The smooth lines are the associated kernel density distribution estimates and are shown for visualisation only.

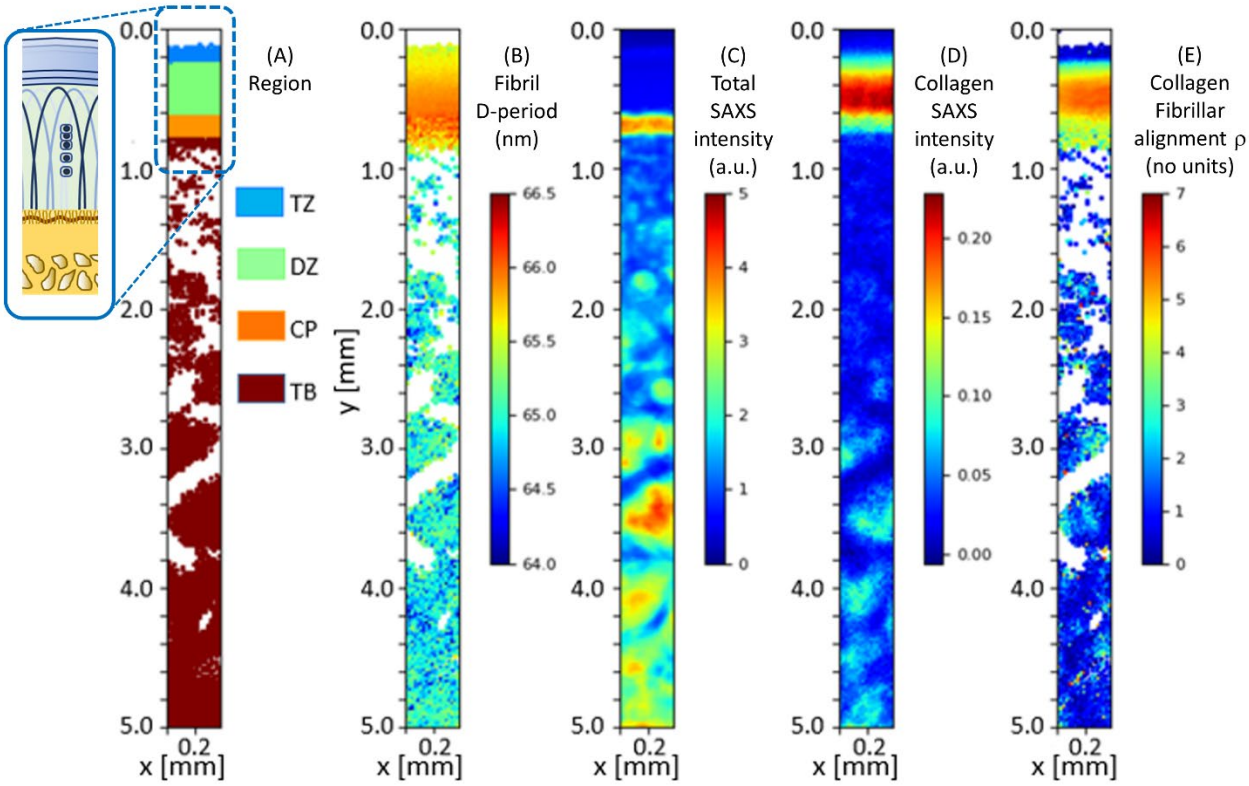

Figure 2

Supplementary Figure 3: Colour map of the depth-wise variation in SAXS derived parameters across bovine bone-cartilage core of 5mm length and 2mm diameter for a full-length scan. This single sample was scanned across a greater depth in the trabecular bone but is otherwise similar to the samples imaged in **Figures 2-3** in the main text. Step size of 20 microns, sample size ~0.38mm width, 5mm length. In this sample we were unable to resolve the thin superficial zone (SZ) at the top. Colour plots display: (A) Regions TZ: transitional zone, DZ: deep zone, CP: calcified plate, and TB: trabecular bone (as in **Figure 1A**, main text), (B) D-period (nm), reflecting collagen pre-strain, (C) total SAXS intensity (a.u.); areas of high intensity correspond to mineral-dense regions, (D) Total SAXS intensity from the background-corrected meridional collagen peak intensity; here, high intensity is observed in articular cartilage and (E) degree of orientation ρ (a.u.), showing high values in the deep zone (DZ), intermediate values in the calcified plate (CP) and transitional zone (TZ), and low values in trabecular bone (TB).

Full-length scan							
Parameter	**Anova**	**Tukey HSD**					
	P value	**Region**	**Diff**	**Lower**	**Upper**	**P adj**	**Signif**
D-period	<2e-16	DZ-CP	-0.1088	-0.1743	-0.0434	0.0001	***
		TB-CP	-0.9740	-1.0306	-0.9174	0.0000	***
		TZ-CP	-0.3628	-0.4471	-0.2786	0.0000	***
		TB-DZ	-0.8651	-0.9034	-0.8268	0.0000	***
		TZ-DZ	-0.2539	-0.3272	-0.1807	0.0000	***
		TZ-TB	-0.6111	0.5457	0.6766	0.0000	***
ρ	<2e-16	DZ-CP	0.74466	-0.8142	2.3074	0.6080	ns
		TB-CP	-1.9789	-3.3292	-0.6284	0.0009	***
		TZ-CP	-3.3334	-5.3429	-1.3240	0.0001	***
		TB-DZ	-2.7255	-3.6387	-1.8122	0.0000	***
		TZ-DZ	-4.0800	-5.8259	-2.3341	0.0000	***
		TZ-TB	-1.3545	-2.9151	0.2060	0.1151	ns
Orientation	0.127	DZ-CP	-3.1012	-14.7246	8.5220	0.9025	ns
		TB-CP	-5.4598	-15.5161	4.5965	0.5021	ns
		TZ-CP	3.1326	-11.8311	18.0964	0.9497	ns
		TB-DZ	-2.3585	-9.1589	4.4418	0.8092	ns
		TZ-DZ	6.2339	-6.7672	19.2350	0.6061	ns
		TZ-TB	8.5924	-3.0289	20.2138	0.2279	ns

Supplementary Table 1: Results from statistical testing of each nanoscale parameter for differences in regions across the BCU for full-length scan. ANOVA tests followed by TUKEY HSD tests were carried out on the data. P values indicate statistical significance, where *** is (p<0.001), ** is (p<0.01), * is (p<0.05) and ns is non-significant difference between regions.

Regular scan			
Parameter	**Sample**	**Anova**	**Signif**
		P value	
D-period	1	<2e-16	***
	2	<2e-16	***
	3	<2e-16	***
	4	<2e-16	***
	5	<2e-16	***
	6	<2e-16	***
ρ	1	4.88E-13	***
	2	4.99E-07	***
	3	5.05E-16	***
	4	0.167	ns
	5	0.00306	**
	6	0.000191	***
Orientation	1	<2e-16	***
	2	0.121	ns
	3	<2e-16	***
	4	<2e-16	***
	5	<2e-16	***
	6	1.45E-15	***

Supplementary Table 2: Results from statistical testing of each nanoscale parameter for differences across tissue regions in the BCU. Data from the 6 regular scan samples. 1-way ANOVA test (with tissue zone as the factor) was carried out on the data, with each scan point labelled as belonging to a specific tissue zone. P values indicate statistical significance, where *** is ($p<0.001$), ** is ($p<0.01$), * is ($p<0.05$) and ns is non-significant difference between regions.

<u>Fibre Diffraction Modelling</u>:

Variation induced by first-moment D-period estimates:

The fibre-diffraction effect described in the Discussion leads to a rightward skew in I(q) (**Figure 9**). Here, we quantify the effect on measured D-period. **Supplementary Figure 4a)** plots radial intensity profiles of the 3rd order peak (after diffuse SAXS background subtraction) from the deep zone (DZ), calcified plate (CP) and trabecular bone (TB) regions from one of the regular 2D scans reported in the paper. **Supplementary Figure 4b)** shows the plots after normalisation to peak height, to show peak shape variations more clearly and correct for the much lower TB peak intensity.

The skew effect is much more pronounced in the cartilaginous (DZ and CP) regions, compared to the bone (TB) tissue. This is consistent with cartilage collagen fibrils being much smaller (larger w_p, **Figure 9**) than bone collage fibrils (e.g., Gottardi et al, *PLOS ONE* 11(10): e0163552; https://doi.org/10.1371/journal.pone.0163552), as w_p is inversely related to the fibril radius.

As a result of the skew, it is clear the first-moment method underestimates the D-period. A complete treatment would need a fitting of the SAXS scattering in both radial and azimuthal directions concurrently via a 3D model. However, to show that the main message of the paper (D-period values in articular cartilage and calcified plate exceed that of trabecular bone) is retained, we use the model sketched in **Figure 9** to quantify the effect as follows:

- The axial width w_a is estimated for the three I(q) curves shown in **Supplementary Figure 4**, by calculating the HWHM for each peak on the left-hand side of the maximum, which is unaffected by the skew (as seen in **Figure 9**).
- For these three values of w_a, three separate curves are rendered in **Supplementary Figure 5a**, showing how skew increases with w_p in each case. The three circles on the plots show the experimentally determined values of skew for the I(q) plots (DZ, CP and TB) in **Supplementary Figure 4**.
- **Supplementary Figure 5b** plots, for these three cases, how the first-moment calculation of D-period varies as the skew increases. The three circles (one for each plot) indicate, likewise, the correction to D-period (note that decrease in D-period is plotted on the abscissa).

Using the information in **Supplementary Figure 5b**, **Supplementary Figure 6** plots the uncorrected and corrected D-period values. Cartilaginous tissue D-period values increase consistently (SZ, TZ, DZ and CP), with the largest increase in the DZ, while trabecular bone values are nearly unchanged (as expected, as its skew is small). This showing that the difference between the unmineralized cartilage and calcified plate versus the trabecular bone is retained. Since we do not discriminate, in the calcified plate, between the calcified cartilage and the subchondral bone in the CP, it is possible the subchondral bone D-period values are lowering the CP average seen in **Supplementary Figure 6**.

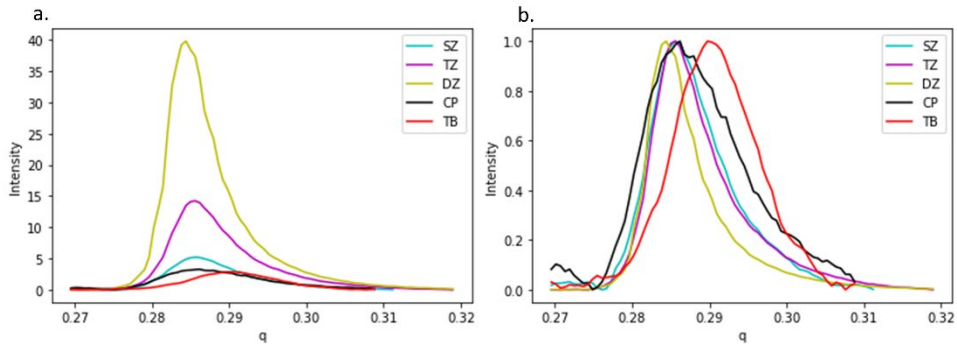

Supplementary Figure 4: (a) Azimuthally integrated I(q) plots from the different tissue zones (SZ, TZ, DZ, CP and TB), corrected for diffuse background. I(q) plots are laterally averaged across sample width at specific vertical depths from cartilage surface; x-axis wavevector *q* is in nm^{-1} (b) Plots from (a) normalized to maximum peak intensity, to show the peak shape variations more clearly.

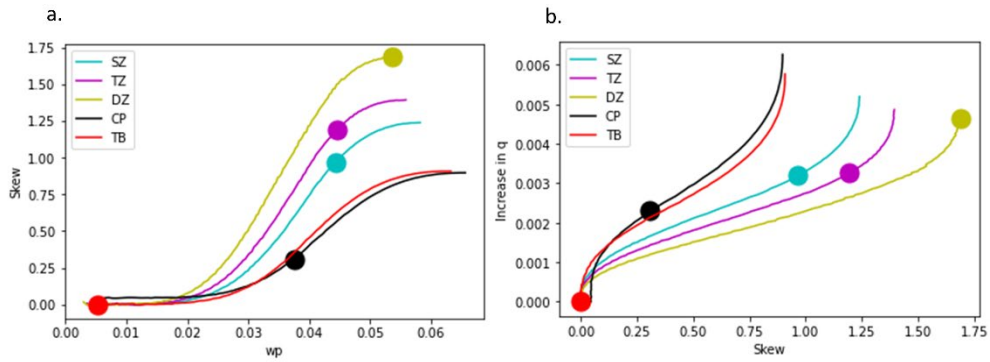

Supplementary Figure 5: (a) Solid lines denote the simulated increase in skew as the equatorial width w_p increases; as w_a is different for each tissue zone, the curves are separate; w_p is in units of nm^{-1}. Filled circles indicate the experimentally determined skew (from **Supplementary Figure 4**) for each zone. (b) The predicted increase in peak position q_0 with skew (in nm^{-1}), as demonstrated in **Figure 9** (main text); solid circles denote the expected increase for different tissue zones, using skew values obtained in (a).

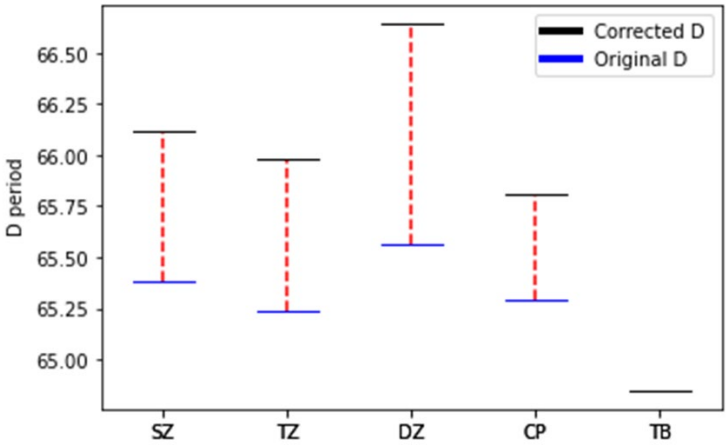

Supplementary Figure 6: Blue bars: D-period (in nm) for the different I(q) curves in **Supplementary Figure 4**, calculated using the first moment of area method used in the main text. Black bars: True D-period, obtained by correcting for the artificial increase in D-period due to the skew, demonstrated in **Supplementary Figure 5b**.

References

1. Goldring SR, Goldring MB. Changes in the osteochondral unit during osteoarthritis: Structure, function and cartilage bone crosstalk. Nature Reviews Rheumatology. 2016. doi:10.1038/nrrheum.2016.148
2. Yuan XL, Meng HY, Wang YC, Peng J, Guo QY, Wang AY, et al. Bone-cartilage interface crosstalk in osteoarthritis: Potential pathways and future therapeutic strategies. Osteoarthritis and Cartilage. 2014. pp. 1077–1089. doi:10.1016/j.joca.2014.05.023
3. James SL, Abate D, Abate KH, Abay SM, Abbafati C, Abbasi N, et al. Global, regional, and national incidence, prevalence, and years lived with disability for 354 Diseases and Injuries for 195 countries and territories, 1990-2017: A systematic analysis for the Global Burden of Disease Study 2017. Lancet. 2018;392. doi:10.1016/S0140-6736(18)32279-7
4. Cui A, Li H, Wang D, Zhong J, Chen Y, Lu H. Global, regional prevalence, incidence and risk factors of knee osteoarthritis in population-based studies. EClinicalMedicine. 2020;29–30. doi:10.1016/j.eclinm.2020.100587
5. Mobasheri A, Henrotin Y. Biomarkers of (osteo)arthritis. Biomarkers. 2015. pp. 513–518. doi:10.3109/1354750X.2016.1140930
6. Liu Z, Meyers MA, Zhang Z, Ritchie RO. Functional gradients and heterogeneities in biological materials: Design principles, functions, and bioinspired applications. Prog Mater Sci. 2017;88: 467–498. doi:10.1016/j.pmatsci.2017.04.013
7. Benninghoff A. Form und Bau der Gelenkknorpel in ihren Beziehungen zur Funktion. Zeitschrift für Zellforsch und Mikroskopische Anat. 1925;2: 783–862.
8. Lu XL, Mow VC. Biomechanics of articular cartilage and determination of material properties. Medicine and Science in Sports and Exercise. 2008. doi:10.1249/mss.0b013e31815cb1fc
9. Inamdar SR, Barbieri E, Terrill NJ, Knight MM, Gupta HS. Proteoglycan degradation mimics static compression by altering the natural gradients in fibrillar organisation in cartilage. Acta Biomater. 2019;97: 437–450. doi:10.1016/j.actbio.2019.07.055
10. Zizak I, Roschger P, Paris O, Misof BM, Berzlanovich A, Bernstorff S, et al. Characteristics of mineral particles in the human bone/cartilage interface. J Struct Biol. 2003;141: 208–217. doi:10.1016/S1047-8477(02)00635-4
11. Finnilä MAJ, Gupta S Das, Turunen MJ, Kestilä I, Turkiewicz A, Lutz-Bueno V, et al. Mineral crystal thickness in calcified cartilage and subchondral bone in healthy and osteoarthritic knees. bioRxiv. 2021; 2021.06.15.448181. doi:10.1101/2021.06.15.448181
12. Gupta HS, Schratter S, Tesch W, Roschger P, Berzlanovich A, Schoeberl T, et al. Two different correlations between nanoindentation modulus and mineral content in the bone-cartilage

775 interface. J Struct Biol. 2005;149. doi:10.1016/j.jsb.2004.10.010
776 13. Weiner S, Traub W. Bone structure: from ångstroms to microns. FASEB J. 1992.
777 doi:10.1096/fasebj.6.3.1740237
778 14. Madi K, Staines KA, Bay BK, Javaheri B, Geng H, Bodey AJ, et al. In situ characterization of
779 nanoscale strains in loaded whole joints via synchrotron X-ray tomography. Nat Biomed Eng.
780 2020;4: 343–354. doi:10.1038/s41551-019-0477-1
781 15. Burr DB, Radin EL. Microfractures and microcracks in subchondral bone: Are they relevant to
782 osteoarthrosis? Rheumatic Disease Clinics of North America. 2003. doi:10.1016/S0889-
783 857X(03)00061-9
784 16. Fratzl P, Weinkamer R. Nature's hierarchical materials. Progress in Materials Science. 2007.
785 doi:10.1016/j.pmatsci.2007.06.001
786 17. Sophia Fox AJ, Bedi A, Rodeo SA. The basic science of articular cartilage: structure,
787 composition, and function. Sports Health. 2009;1: 461–468.
788 18. Inamdar SR, Knight DP, Terrill NJ, Karunaratne A, Cacho-Nerin F, Knight MM, et al. The Secret
789 Life of Collagen: Temporal Changes in Nanoscale Fibrillar Pre-Strain and Molecular
790 Organization during Physiological Loading of Cartilage. ACS Nano. 2017;11: 9728–9737.
791 doi:10.1021/acsnano.7b00563
792 19. Tadimalla S, Tourell MC, Knott KI, Momot KI, Knott R, Momot KI. Quantifying collagen fibre
793 architecture in articular cartilage using small-angle X-ray scattering. Biomed Spectrosc
794 Imaging. 2017;6: 37–57. doi:10.3233/BSI-170164
795 20. Fang M, Goldstein EL, Turner AS, Les CM, Orr BG, Fisher GJ, et al. Type i collagen D-spacing in
796 fibril bundles of dermis, tendon, and bone: Bridging between nano- and micro-level tissue
797 hierarchy. ACS Nano. 2012. doi:10.1021/nn302483x
798 21. Zimmermann EA, Schaible E, Bale H, Barth HD, Tang SYY, Reichert P, et al. Age-related
799 changes in the plasticity and toughness of human cortical bone at multiple length scales. Proc
800 Natl Acad Sci U S A. 2011;108: 14416–14421. doi:10.1073/pnas.1107966108
801 22. Bell JS, Hayes S, Whitford C, Sanchez-Weatherby J, Shebanova O, Vergari C, et al. The
802 hierarchical response of human corneal collagen to load. Acta Biomater. 2018;65: 216–225.
803 doi:10.1016/j.actbio.2017.11.015
804 23. Gautieri A, Passini FS, Silvan U, Guizar-Sicairos M, Carimati G, Volpi P, et al. Advanced
805 glycation end-products: Mechanics of aged collagen from molecule to tissue. Matrix Biol.
806 2016.
807 24. Leighton MP, Rutenberg AD, Kreplak L. D-band strain underestimates fibril strain for twisted
808 collagen fibrils at low strains. J Mech Behav Biomed Mater. 2021.

809 doi:10.1016/j.jmbbm.2021.104854
810 25. Bhosale AM, Richardson JB. Articular cartilage: structure, injuries and review of management.
811 Br Med Bull. 2008;87: 77–95. doi:10.1093/bmb/ldn025
812 26. Masic A, Bertinetti L, Schuetz R, Chang S-W, Metzger TH, Buehler MJ, et al. Osmotic Pressure
813 Induced Tensile Forces in Tendon Collagen. Nat Commun. 2015;6: 5942.
814 doi:10.1038/ncomms6942
815 27. Fang W, Ping H, Wagermaier W, Jin S, Amini S, Fratzl P, et al. Rapid collagen-directed
816 mineralization of calcium fluoride nanocrystals with periodically patterned nanostructures.
817 Nanoscale. 2021. doi:10.1039/d1nr00789k
818 28. Lees S. Mineralization of type I collagen. Biophys J. 2003. doi:10.1016/S0006-3495(03)74466-
819 X
820 29. Temple DK, Cederlund AA, Lawless BM, Aspden RM, Espino DM. Viscoelastic properties of
821 human and bovine articular cartilage: a comparison of frequency-dependent trends. BMC
822 Musculoskelet Disord. 2016. doi:10.1186/s12891-016-1279-1
823 30. Burgin L V., Aspden RM. Impact testing to determine the mechanical properties of articular
824 cartilage in isolation and on bone. J Mater Sci Mater Med. 2008. doi:10.1007/s10856-007-
825 3187-2
826 31. Smith AJ, Alcock SG, Davidson LS, Emmins JH, Hiller Bardsley JC, Holloway P, et al. I22:
827 SAXS/WAXS beamline at Diamond Light Source - an overview of 10 years operation. J
828 Synchrotron Radiat. 2021;28: 939–947. doi:10.1107/S1600577521002113
829 32. Henrich B, Bergamaschi A, Broennimann C, Dinapoli R, Eikenberry EF, Johnson I, et al.
830 PILATUS: A single photon counting pixel detector for X-ray applications. Nucl Instruments
831 Methods Phys Res Sect A Accel Spectrometers, Detect Assoc Equip. 2009;607.
832 doi:10.1016/j.nima.2009.03.200
833 33. Filik J, Ashton AW, Chang PCY, Chater PA, Day SJ, Drakopoulos M, et al. Processing two-
834 dimensional X-ray diffraction and small-angle scattering data in DAWN 2. J Appl Crystallogr.
835 2017;50: 959–966. doi:10.1107/S1600576717004708
836 34. Gourrier A, Wagermaier W, Burghammer M, Lammie D, Gupta HS, Fratzl P, et al. Scanning X-
837 ray imaging with small-angle scattering contrast. J Appl Crystallogr. 2007;40.
838 doi:10.1107/S0021889807006693
839 35. Blowes LM, Egertová M, Liu Y, Davis GR, Terrill NJ, Gupta HS, et al. Body wall structure in the
840 starfish Asterias rubens. J Anat. 2017;231. doi:10.1111/joa.12646
841 36. Liebi M, Georgiadis M, Menzel A, Schneider P, Kohlbrecher J, Bunk O, et al. Nanostructure
842 surveys of macroscopic specimens by small-angle scattering tensor tomography. Nature.

2015;527: 349–352. doi:10.1038/nature16056

37. Fratzl P. Collagen: Structure and Mechanics. Fratzl P, editor. Collagen: Structure and Mechanics. Springer US; 2008. doi:10.1007/978-0-387-73906-9

38. Xi L, De Falco P, Barbieri E, Karunaratne A, Bentley L, Esapa CT, et al. Bone matrix development in steroid-induced osteoporosis is associated with a consistently reduced fibrillar stiffness linked to altered bone mineral quality. Acta Biomater. 2018;76. doi:10.1016/j.actbio.2018.05.053

39. Yang W, Sherman VR, Gludovatz B, Schaible E, Stewart P, Ritchie RO, et al. On the tear resistance of skin. Nat Commun. 2015;6: 6649. doi:ARTN 6649 10.1038/ncomms7649

40. Almer JD, Stock SR. Internal strains and stresses measured in cortical bone via high-energy X-ray diffraction. J Struct Biol. 2005;152: 14–27. doi:10.1016/j.jsb.2005.08.003

41. Xi L, Zhang Y, Gupta H, Terrill N, Wang P, Zhao T, et al. A multiscale study of structural and compositional changes in a natural nanocomposite: Osteoporotic bone with chronic endogenous steroid excess. Bone. 2020. doi:10.1016/j.bone.2020.115666

42. Newville M, Otten R, Nelson A, Ingargiola A, Stensitzki T, Allan D, et al. lmfit/lmfit-py 1.0.2. Zenodo; 2021. doi:10.5281/zenodo.4516651

43. Karunaratne A, Xi L, Bentley L, Sykes D, Boyde A, Esapa CT, et al. Multiscale alterations in bone matrix quality increased fragility in steroid induced osteoporosis. Bone. 2016;84: 15–24. doi:10.1016/j.bone.2015.11.019

44. Xi L, De Falco P, Barbieri E, Karunaratne A, Bentley L, Esapa CT, et al. Reduction of fibrillar strain-rate sensitivity in steroid-induced osteoporosis linked to changes in mineralized fibrillar nanostructure. Bone. 2020;131. doi:10.1016/j.bone.2019.115111

45. Pabisch S, Wagermaier W, Zander T, Li C, Fratzl P. Chapter Eighteen - Imaging the Nanostructure of Bone and Dentin Through Small- and Wide-Angle X-Ray Scattering. In: De Yoreo JJBT-M in E, editor. Research Methods in Biomineralization Science. Academic Press; 2013. pp. 391–413. doi:https://doi.org/10.1016/B978-0-12-416617-2.00018-7

46. Hunter JD. Matplotlib: A 2D graphics environment. Comput Sci Eng. 2007;9: 90–95. doi:10.1109/MCSE.2007.55

47. Fratzl P, Misof K, Zizak I, Rapp G, Bernstorff S, Amenitsch H. Fibrillar Structure and Mechanical Properties of Collagen. J Struct Biol. 1997;122: 119–122. doi:10.1006/jsbi.1998.3966

48. Fratzl P, Fratzl-Zelman N, Klaushofer K. Collagen packing and mineralization. An x-ray scattering investigation of turkey leg tendon. Biophys J. 1993. doi:10.1016/S0006-3495(93)81362-6

49. Tozzi G, Fernández MP, Davis S, Karali A, Kao AP, Blunn G. Full-field strain uncertainties and

residuals at the cartilage-bone interface in unstained tissues using propagation-based phase-contrast XCT and digital volume correlation. Materials (Basel). 2020. doi:10.3390/ma13112579

50. Guinier A, Fournet G. Small-Angle Scattering of X-rays. John Wiley & Sons Ltd.; 1955.

51. Khanarian NT, Boushell MK, Spalazzi JP, Pleshko N, Boskey AL, Lu HH. FTIR-I compositional mapping of the cartilage-to-bone interface as a function of tissue region and age. J Bone Miner Res. 2014. doi:10.1002/jbmr.2284

52. Moger CJ, Barrett R, Bleuet P, Bradley DA, Ellis RE, Green EM, et al. Regional variations of collagen orientation in normal and diseased articular cartilage and subchondral bone determined using small angle X-ray scattering (SAXS). Osteoarthr Cartil. 2007;15: 682–7. doi:10.1016/j.joca.2006.12.006

53. Liebi M, Georgiadis M, Kohlbrecher J, Holler M, Raabe J, Usov I, et al. Small-angle X-ray scattering tensor tomography: Model of the three-dimensional reciprocal-space map, reconstruction algorithm and angular sampling requirements. Acta Crystallogr Sect A Found Adv. 2018;A74: 12–24. doi:10.1107/S205327331701614X

54. Giannini C, De Caro L, Terzi A, Fusaro L, Altamura D, Diaz A, et al. Decellularized pericardium tissues at increasing glucose, galactose and ribose concentrations and at different time points studied using scanning X-ray microscopy. IUCrJ. 2021;8: 621–632. doi:10.1107/S2052252521005054

55. Qin HJ, Xu T, Wu HT, Yao ZL, Hou YL, Xie YH, et al. SDF-1/CXCR4 axis coordinates crosstalk between subchondral bone and articular cartilage in osteoarthritis pathogenesis. Bone. 2019;125. doi:10.1016/j.bone.2019.05.010

56. Findlay DM, Kuliwaba JS. Bone-cartilage crosstalk: A conversation for understanding osteoarthritis. Bone Research. 2016. doi:10.1038/boneres.2016.28